Pergamon

Radiat. Phys. Chem. Vol. 45, No. 3, pp. 459–481, 1995

0969-806X/95 $9.50 + 0.00

GEOLOGICAL APPLICATIONS OF SYNCHROTRON RADIATION

C. M. B. HENDERSON,[1] G. CRESSEY[2] and S. A. T. REDFERN[1,3]

[1]Department of Geology, University of Manchester, Manchester M13 9PL, [2]Department of Mineralogy, The Natural History Museum, Cromwell Road, London SW7 5BD and [3]Department of Chemistry, University of Manchester, Manchester M13 9PL, U.K.

Abstract—Synchrotron-based, Earth sciences research carried out over the last 5 years is reviewed with special attention being given to X-ray absorption studies; X-ray diffraction and X-ray fluorescence microprobe applications are considered more briefly. A comprehensive bibliography is included. The main part of the paper summarizes recent work carried out at the Daresbury SRS.

K-edge XAS studies of glasses as models for silicate melts provide information on the local structural environments of Si, Fe^{2+} and Fe^{3+}. By analogy with synthetic "leucites" which contain Fe^{2+} and Fe^{3+} in tetrahedral framework sites, it seems that many model glasses also contain both oxidation states of Fe in the network, rather than as network modifiers. The structural sites occupied by the minor elements Mn, Zn and Ti in staurolite have been identified using XAFS; Mn and Zn substitute for Fe^{2+} in the tetrahedral *T*2 site, while Ti occupies the distorted *M*2 octahedral site. L-edge spectroscopy is used to identify the valencies and electronic structures of Mn and Fe in minerals and the $Fe^{2+}:Fe^{3+}$ ratio in a natural spinel is determined. The polarized nature of the synchrotron beam is exploited in determining the Fe X-ray absorption anisotropy in single crystal tourmaline and epidote.

XRD powder studies include Rietveld-refinement structure determination and compressibility studies. Synthetic "leucites" having the stoichiometry $K_2MgSi_5O_{12}$ have distinctly different structures. The dry-synthesized form is cubic Ia3d with Si and Mg fully disordered on tetrahedral framework sites, while the hydrothermally-synthesized polymorph is monoclinic $P2_1/c$ with Si and Mg fully disordered on, respectively, 10 and 2 tetrahedral sites. The reversible tetragonal to orthorhombic phase transition in gillespite ($BaFeSi_4O_{10}$) has been studied in a diamond anvil cell using ED detection and found to occur at 1.2 ± 0.1 GPa. The anomalous compressibility observed has been interpreted in terms of ferroelastic and coelastic phenomena and the related order parameters analysed using Landau theory. The compressibility of $MgCO_3$, determined up to 20 GPa, has been combined with thermochemical data to obtain an "equation of state" for magnesite and it is found that magnesite is likely to be the main host for carbon in the Earth's lower mantle.

INTRODUCTION

In a stimulating early review, Calas *et al.* (1984) summarized the properties of synchrotron radiation (SR) and emphasized the mineralogical applications of synchrotron-based X-ray absorption spectroscopy (XAS) (see Charnock, pp. 385–391; and Johnston and Wells, pp. 393–412, this issue), energy dispersive X-ray diffraction (XRD) (see Cernik and Barnes, pp. 445–457, this issue), small-angle scattering, X-ray microradiography, and X-ray topography. However, with the exception of a few very active and expanding research groups, Earth scientists have not become such avid users of SR as their "cousins" working in mainstream materials science. Nevertheless, the active workers have taken full advantage of the unique properties of SR applying them to wide-ranging areas including: XAS of crystals, glasses and solutions; X-ray powder and single-crystal diffraction under ambient and high-pressure and/or high-temperature conditions; and X-ray fluorescence microprobe analyses for trace elements. In this review we will briefly cover the current wide scope of Earth science research, except that work on zeolites, clays and other natural minerals, performed in relation to their catalytic properties, will not be included. We have attempted to reference work published over the last 5 years as comprehensively as possible. We will then present some of our own recent work carried out at the S.E.R.C. Daresbury Synchrotron Radiation Source (SRS).

SCOPE OF EARTH SCIENCE RESEARCH

X-ray absorption spectroscopy

In early work, Extended X-ray Absorption Fine Structure Spectroscopy (XAFS) and X-ray Absorption Near Edge Structure (XANES) were used to investigate the structural environments of major elements in "model-compound" minerals (e.g. Waychunas *et al.*, 1983; Calas and Petiau, 1983a) and in glasses as models for silicate melts (e.g. Calas and Petiau, 1983b; Binsted *et al.*, 1985, 1986). Much of the earlier work has been summarized in the excellent reviews of Calas *et al.* (1987) and Brown *et al.* (1988). Since then, XAS has been used in many diverse research programmes (e.g. Henderson *et al.*, 1991) as summarized below.

Cressey and Steel (1988) studied synthetic epidotes and found that three different sites are involved in accommodating rare earth elements (REE), and that site preference is a function of REE size. Gd is mainly located in the 10-coordinate *A*2-type sites, Er in 9-coordinate *A*1, and Lu in the smaller *M*3-type octahedral sites. Charnock *et al.* (1988, 1989a, b) studied natural and synthetic members of the chemically and structurally complex tetrahedrite mineral group by Cu, Ag, Fe, Cd and Sb XAFS. They showed that Cu (assumed to be mainly Cu^+) preferentially occupies a tetrahedral site implying that Ag mainly occupies a three-coordinated site. More recently, van der Laan *et al.* (1992) and Pattrick *et al.* (1993) have used 2p Cu XAS to show that tetrahedrites also contain Cu^{2+}. Charnock *et al.* (1990) also studied thiospinels by Cr, Fe, Co, Ni, and Cu XAFS and showed that carrollite ($CuCo_2S_4$) has Cu wholly in the tetrahedral sites and that daubréelite ($FeCr_2S_4$) is a normal spinel. Guttler *et al.* (1989) studied heated Fe-rich biotite by Fe and Ti K-edge XAS and concluded that thermally-activated hopping conduction according to $Fe^{2+}Ti^{4+} \rightarrow Fe^{3+}Ti^{3+}$ is not a significant process during thermal deprotonation and oxidation. Quartieri *et al.* (1993) studied the local symmetry of Fe in the 8-fold coordination sites in garnets. Paris *et al.* (1993) found that Ti in synthetic richterites occurs in 4-coordination. Manceau (1990) studied Ni in phyllosilicates and concluded that it did not substitute for Mg randomly but occurred in clusters of mean size $>$20–30 Å. McKeown (1989) compared experimental Al K-edge XANES spectra for albite, nepheline, jadeite, corundum and sillimanite to calculated spectra, while Behrens *et al.* (1991) have related changes in Ti K-edge XANES spectra to varying structural environments for a wide range of minerals. Mottana *et al.* (1991) used XANES spectra to show that Fe^{2+} exists in two sites in orthopyroxenes. Pingitore *et al.* (1991) showed that the Sr environment in calcite was more akin to that of Ca in calcite than to Sr in strontianite. McKeown (1991) compared calculated and experimental K-edge XANES spectra for Cu, Fe and Zn in chalcopyrite ($CuFeS_2$) and sphalerite (ZnS) and obtained reasonably good agreement. Sainctavit *et al.* (1986, 1987, 1990) used combinations of S, Cu and Zn K-edges, Cu L-edges and multiple scattering calculations to deduce electronic structures of chalcopyrite and sphalerite. Schofield *et al.* (1993) have found that Cu L-edge spectroscopy can be used to identify two distinctly different Cu electronic environments in $(Cu,Zn)WO_4$ solid solutions.

The linear polarization of the synchrotron beam has been exploited by using oriented single crystals to study the anisotropic properties of Fe K-edge absorption in biotite and chlorite (Manceau *et al.*, 1988, 1990a) and Fe-diaspore (Hazeman *et al.*, 1992). Waychunas and Brown (1990) determined Fe and Ti K-edge spectra for oriented single crystals of gillespite (square planar Fe^{2+}), anatase (octahedral Ti), and epidote (distorted octahedral Fe^{3+} in the *M*3-type site). As expected, the XANES features were found to be distinctly polarization dependent.

XAS studies of natural and synthetic amorphous precipitates of 3d transition elements have provided new information on their short-range structures and valencies. Manceau *et al.* (1987; cf. also Manceau and Combes, 1988; Manceau, 1989) studied K-edge XAS of Mn, Co and Ni in manganese oxides from laterites: Mn^{4+} and Co^{3+} are in similar sites but the environment of Ni^{2+} is quite different. Manceau *et al.* (1990b; 1992a, b) have further extended this work on manganese hydrous oxides. Combes *et al.* (1989 and 1990) determined the local environments of Fe^{3+} at different stages in the precipitation of hydrous oxide gels and during subsequent ageing. Fe in solution and in the precipitates remains in 6-coordination throughout. The fresh precipitate shows outer shells, due to Fe–Fe correlations, at 3.45 Å (corner-sharing octahedra) and 3.06 Å (edge-sharing) but after 1.5 h ageing at 92°C a new shell appears at 2.89 Å (face-sharing octahedra). This species disappears after 6 h with the nucleation and growth of hematite. Bidoglio *et al.* (1993) studied the surface redox transformations of thallium and chromium on colloidal Mn and Fe hydrated oxides.

XAS work has also been started on element complexing in aqueous electrolyte solutions. Farges *et al.* (1991b; 1993) have found that Au(III) in 1 M NaCl at $pH = 2$ is square planar, coordinated by 4 Cl but that the Cl:O ratio of the ligands increases with increasing pH. Helz *et al.* (1993) studied Cu and Zn bisulphide complexes in NaHS solutions. The predominant soluble Cu complex is believed to be a polynuclear $(Cu_4S_6)^{2-}$ cluster, which has tetrahedral Cu with S bridges along the six tetrahedron sides. Work has recently been started at Daresbury in which solutions are sealed in silica tubes and spectra obtained at temperatures up to 300°C. In the first experiments, Seward *et al.* (1993) studied 0.1 M solutions of $CdCl_2$ and found that the number of Cl ligands in the aquated Cd-complex increased with increasing T to 250°C and increasing Cl molality. Seward and Henderson (1992) investigated 0.1 M $AgNO_3$ at temperatures from 25 to 300°C and have found that the Ag is tetrahedrally coordinated by O and that the Ag–O first shell distance decreases with temperature as a result of the solution becoming more associated. Other work on amorphous systems has included the characterization of "major-" and "trace-element" environments in silicate glasses: Si (Davoli *et al.*, 1992); Fe (Binsted *et al.*, 1986; Waychunas *et al.*, 1988; Jackson *et al.*, 1991); Ca (Binsted *et al.*, 1985; Combes *et al.*, 1991); rare earth elements (Ponader and Brown, 1989a, b); Mn and Sr (Kohn *et al.*, 1990); Zr (Farges *et al.*, 1991a); Ni (Galoisy and

Calas, 1991, 1992, 1993a, b); and U (Farges *et al.*, 1992). Nakai *et al.* (1987) used K-edge XANES and XAFS to characterize Zr and Nb environments in several metamict (amorphous due to radiation damage) minerals while Farges and Calas (1991) determined how the local environments of Zr, Th and U in zircon and thorite change as a function of metamictization. Zhang and Boduszynski (1991) found that V in heavy petroleum residues has a similar structure to that in a porphyrin complex. In addition, the structural nature of sulphur species (elemental, reduced and oxidized) in heavy petroleums and source rocks has been determined using XANES (Waldo *et al.*, 1991); a similar approach has also been applied to S in coal (Huggins *et al.*, 1991).

XAS studies of wet samples to determine the structure of metal complexes adsorbed on mineral surfaces are becoming of increasing importance in environmental geochemistry. Chisholm-Brause *et al.* (1990a) studied adsorption of Co^{2+} on γ-alumina, rutile (TiO_2) and kaolinite ($Al_2Si_2O_5(OH)_4$) and found direct evidence for the presence of polynuclear inner-sphere complexes at surface coverages less than one monolayer. Chisholm-Brause *et al.* (1990b) studied adsorption of Pb^{2+} on γ-alumina and suggested that the adsorbed complex was mono-dentate and inner-sphere in type. Waychunas *et al.* (1991, 1993) studied adsorption of arsenate (AsO_4) on ferrihydrite, goethite, akangéite and lepidocrocite and found clear evidence for the presence of an inner sphere, bidentate arsenate complex. They also reported on the kinetics of arsenate adsorption and coprecipitation (Fuller *et al.*, 1993).

In situ high-P/T XAS studies have recently been reported. Seifert *et al.* (1993) developed a furnace to allow *in situ* XAS to 1500°C, reporting a good signal at the Ti edge of $K_2TiSi_4O_{11}$ glasses and melts even at very high T. Andrault and Poirier (1991) obtained Zr and Ge K-edge spectra using energy dispersive detection in a diamond cell to study distortions of perovskites ($BaZrO_3$, $SrZrO_3$ and $CaGeO_3$) under pressure and Andrault *et al.* (1992) determined the compressibilities of GeO_4 tetrahedra in $MgGeO_3$ enstatite and $CaGeO_3$ wollastonite. Andrault *et al.* (1993) subsequently measured the changes in Ge coordination by O as a function of combined P and T in GeO_2 (quartz-analogue) held in a heating diamond anvil cell. The design of high-P XAS experiments undertaken at LURE is discussed in more detail in Itié (1992).

X-ray diffraction

The special properties of SR have provided new opportunities in X-ray crystallography (e.g. Prewitt *et al.*, 1987; Cernik and Barnes, pp. 445–457, this issue). In particular, the ability to focus or collimate the intense beam allows very small crystals or powdered samples to be studied; this is especially useful for high-pressure studies using diamond anvil cells (see Nelmes and McMahon, 1994). Use of the high-energy "white" beam with ED detection expedites much *in situ*, high-T and high-P work and is of particular importance in studies of the Earth's mantle and core. In particular, large volume, multi-anvil apparati have been stationed at wiggler ports on many sources and employed for high-P/T mineral physics research (Kikegawa, 1992; Weidner *et al.*, 1992). In addition, ED detection allows rapid collection of diffraction data providing kinetic information. Moreover, the low beam divergence and the ability to tune the beam to give truly monochromatic radiation provides narrow peak widths with good signal-to-noise ratio and the possibility of determining structures of powdered samples using Rietveld peak deconvolution techniques (Rietveld, 1969).

Kudoh *et al.* (1990) determined the structure of a synthetic $(Mg,Fe)SiO_3$ perovskite (quenched from 26 GPa and 2173 K) using a single crystal of dimensions $29 \times 29 \times 43\,\mu m$ and monochromatic radiation. They found that Fe (and Cr) substitutes for Mg in the 8–12 coordinated site rather than for Si in the octahedral site, and that about 2% of the total Mg occurs in the latter site. Diamond anvil cell, "white-beam" ED studies of powdered samples of $(MgFe)_2SiO_4$-β-spinel (Fei *et al.*, 1992a), magnesiowustite (Mg,Fe)O (Fei *et al.*, 1992b), and metallic $Fe_{0.8}Ni_{0.2}$ alloy (Mao *et al.*, 1990), and of a polycrystalline sample of $(Mg,Fe)SiO_3$ perovskite using monochromatic radiation (Mao *et al.*, 1991), have provided crucial equation-of-state (EOS) information for these phases in the Earth's mantle or core. In addition, Fei and Mao (1993) have used similar techniques to measure temperature dependence of the static compression of brucite ($Mg(OH)_2$) to 35 GPa at 300 K and to 80 GPa at 600 K. These data were used to deduce the dehydration curve of brucite up to 55 GPa, and to suggest that the existing EOS for fluid H_2O may overestimate its volume at pressures above 50 GPa.

The high-resolution obtained with monochromatic radiation, combined with Rietveld refinement, are being used increasingly for structure determination of polycrystalline synthetic "minerals" and natural phases which are too scarce and/or fine-grained for single crystal study; e.g. synthetic forsterite (Cernik *et al.*, 1990), and the natural mineral perlialite (Artioli and Kvick, 1990). Such techniques are also invaluable in studying peak-splitting associated with ordering and/or phase transformations, e.g. cordierite (Putnis *et al.*, 1987; Redfern *et al.*, 1989) and albite (Salje, 1992).

X-ray fluorescence microprobe

High-intensity, plane-polarized SR can provide a probe with very low background, ideal for XRF trace element analysis. By using multilayer mirrors with Kirkpatrick–Baez mirror geometry, focused synchrotron beams have been obtained with spot size 5–10 μm diameter. This set-up, usually with ED detection, has been applied to a number of research programmes where fine spatial resolution and non-destructive analysis are important requirements. Samples analysed include: fluid inclusions (Frantz *et al.*, 1988; Rankin *et al.*, 1992); feldspars (Lu *et al.*, 1989); sulphides in coal (White *et al.*, 1989); carbonates (Kopp *et al.*, 1990); stratospheric cosmic dust (Flynn and Sutton, 1990); pantellerite glass (Rivers *et al.*, 1991). In a recent extension of this approach, a monochromator has been incorporated allowing XANES features to be scanned for concentration levels down to several hundred ppm. In this way, Hayakawa *et al.* (1991) have obtained 900 × 900 μm scanned images (10 μm steps) of Cr, Fe, Ni and Zn in peridotite, and Sutton *et al.* (1993) have detected predominant Cr^{2+} in 200 μm regions of lunar olivines and Cr^{3+} in lunar pyroxenes.

REVIEW OF EARTH SCIENCES RESEARCH AT DARESBURY

In the sections below we will review recent XAS and XRD Earth science research carried out at the SRS. The topics included range from silicate glass/melt structures to single crystal polarized XANES and from powder structure determination to mineral compressibility.

Silicate glass/melt structures studied by XAS

To rigorously model magmatic processes, structural information for melts is necessary so that the factors controlling phase relations, diffusion rates, and viscosities can be understood. Such information is much easier to obtain if quenched glasses are studied as models for melt structure. Silicate melts consist of a network of SiO_4 (and AlO_4) tetrahedra linked (polymerized) to adjacent tetrahedra by bridging oxygens. Network modifiers reduce the linkage forming non-bridging oxygens. Melt viscosity is higher the greater the degree of polymerization. The low field strength elements Na, K, and Ca are likely to be the main network modifiers in natural magmas, depending on their concentrations relative to Al. The roles of other elements such as Ti, Mg, Fe^{2+}, Fe^{3+}, Mn are much less clear but most petrologists assume that Ti is a network former and that Fe, Mg and Mn are network modifiers.

Si XANES and XAFS spectra

Si K-edge spectra have been obtained for a series of crystalline model compounds of varying structural complexities as well as a range of glass compositions including some hydrous and high-pressure varieties.

Rock-forming silicates contain Si in 4-coordination although the SiO_4 tetrahedron shows varying degrees of distortion in different minerals. The inter-sample range of Si–O tetrahedral distances varies from about 1.57 to 1.69 Å. Based on these values and on the invariant coordination number, the Si EXAFS should only show limited variation as far as the first shell is concerned. Both the periodicities and amplitudes of the EXAFS should be fairly constant. However, the XANES spectra would be expected to show important differences depending on the degree of polymerization of the tetrahedra (i.e. the proportion of bridging to non-bridging oxygens). Figure 1(a) shows that this is indeed the case for the series monomer–dimer–chain–framework (forsterite–akermanite–diopside–anorthite). In addition the XANES varies depending on the precise topology of

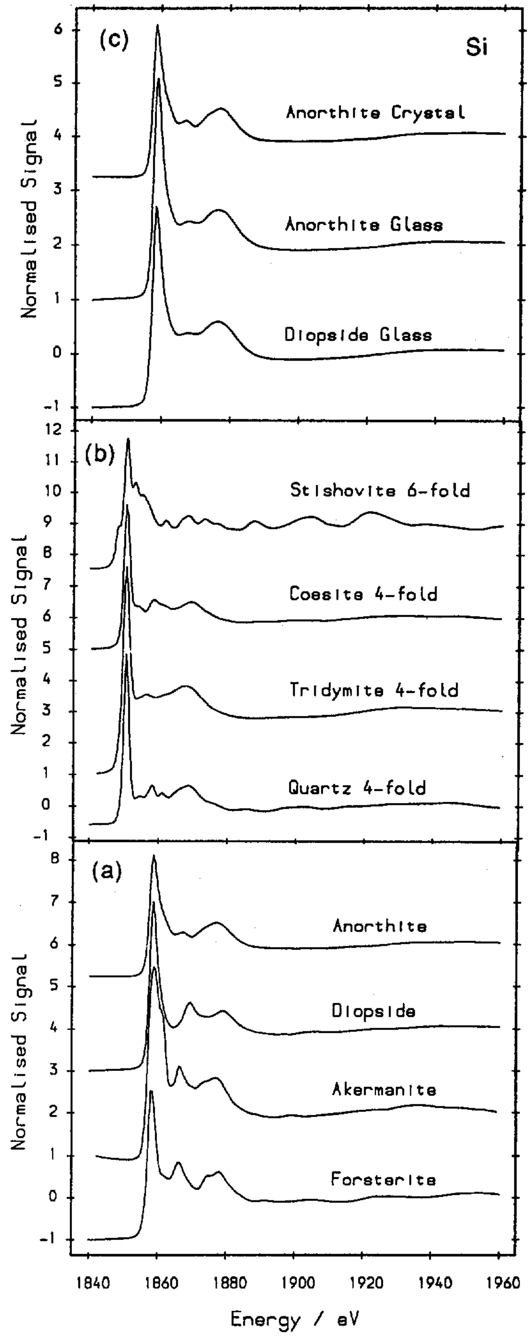

Fig. 1. Si K-edge XANES spectra for: (a) minerals with different degrees of SiO_4 polymerization—monomer, forsterite (Mg_2SiO_4)–dimer, akermanite ($Ca_2MgSi_2O_7$)–single chain, diopside ($CaMgSi_2O_6$)–network, anorthite ($CaAl_2Si_2O_8$); (b) silica polymorphs; (c) crystalline anorthite–anorthite glass–diopside glass.

the framework [Fig. 1(b)] and on the nature of the cavity cations. As would be expected, major differences occur between the XANES for 4-coordinated and 6-coordinated Si [e.g. stishovite, Fig. 1(b)].

First shell Si–O distances refined from the EXAFS for representative model compounds are given in Table 1; excellent agreement is shown between the present data and average values from crystal structure determinations. There is a trend of decreasing average Si–O bond length with decreasing numbers of non-bridging oxygens (i.e. O coordinated to "non-network" Mg, Fe^{2+} and Ca). In crystalline gehlenite ($Ca_2Al(Al,Si)_2O_7$), pairs of tetrahedra (containing Si and Al) are linked by "non-network" 4-coordinated Al, building up a "framework-like" structure. Thus the Si–O distance in gehlenite is more similar to that of anorthite than to those of forsterite and diopside (Table 1).

In SiO_2 glass the Si K-edge Fourier Transform (FT) is dominated by a peak at 1.61 Å; this peak is due to interactions with the nearest neighbour O shell i.e. the SiO_4 tetrahedron. This peak is narrow with a Debye–Waller factor (D.W.) of 0.004 $Å^2$, reflecting the generally well-ordered Si local environment. The comparative data for crystalline quartz are $R = 1.613$ Å and D.W. $= 0.002$ $Å^2$ (static disorder only). A small second shell peak in the FT is due to Si—Si correlations. Although the EXAFS information is one-dimensional (radial), the Si–O–Si bond angle in SiO_2 glass can be estimated from the first shell Si-O and the second shell Si–Si distances (about $160 \pm 20°$).

The Si–O data for several different glasses (Table 1) range from 1.606 to 1.631 Å and this difference is believed to be real (relative distances accurate to about ± 0.01 Å). Anorthite crystal and glass have closely similar Si–O distances as do crystals and glasses of gehlenite and quartz compositions reflecting the similarities between the framework crystal structures and the equivalent glass networks. In contrast the diopside glass has a slightly shorter Si–O than the crystal and is similar to that of gehlenite glass. Differences between different glasses reflect the nature of the other framework and modifying cations and of framework topology (i.e. ring size variation and bond-angle distribution).

The Debye–Waller data in Table 1 show that the glasses have consistently smaller D.W. factors for the first shell of oxygens around Si than the equivalent crystalline materials; the crystals seem to be more disordered than the glasses! The explanation for this is due to glasses being able to adopt more symmetrical tetrahedral SiO_4 configurations than the crystals because the latter are constrained to have long range translational symmetry. Thus the disorder in the glass has been taken up in producing a more variable distribution of bridging bond angles than that of the crystal.

The XANES for glasses are very similar irrespective of composition and whether the glasses are hydrous or anhydrous. These spectra are closely similar to those of crystalline tridymite and anorthite [cf. Figs 1(a), (b) and (c)] even though tridymite has 6-rings of tetrahedra while anorthite has 4-rings. These minerals are similar in having multiple Si sites with a range of Si–O distances and distortions. Thus their XANES and those of the glasses reflect such distortions rather than the nature of the ring-structures (N.B. the absorption spectra give an average environment).

Structural environments of iron in glasses and crystalline model compounds

An understanding of the structural role of iron in silicate melts is important not only in accounting for rheological and diffusion properties and phase relations, but also because of the significance of redox ratios as oxygen fugacity (fO_2) indicators. A variety of glasses, prepared at different fO_2 conditions, together with natural basalt and obsidian and pantellerite glasses (glassy "granites"), have been studied by Fe K-edge XAS. Silicate minerals with Fe in either 2+ or 3+ oxidation states and in 4-, 6- or 8-fold coordination have been run as model compounds; synthetic "leucites" ($KFe^{3+}Si_2O_6$ and $K_2Fe^{2+}Si_5O_{12}$) were used as models for 4-fold ferric and ferrous iron

Table 1. Refined first shell Si data

Sample	R(Å)	N (refined)	D.W.	Crystallography Mean (1σ SD)
Crystalline model compounds				
Forsterite	1.633	4.2	0.004	1.636 (0.017)
Fayalite	1.631	4.2	0.003	1.636 (0.012)
Gehlenite	1.614	3.4	0.004	1.620 (0.023)
Diopside	1.635	3.6	0.006	1.635 (0.05)
Anorthite	1.611	4.1	0.003	1.613 (0.03)
Quartz	1.613	4.0	0.002	1.609 (0.003)
Aegirine ($NaFe^{3+}Si_2O_6$)	—	—	—	1.627 (0.021)
Glasses				
"Gehlenite"	1.621	3.4	0.003	
"Diopside"	1.624	3.8	0.002	
"Anorthite"	1.606	4.2	0.002	
"SiO_2"	1.613	4.0	0.001	
"Aegirine"	1.631	3.6	0.001	

R = bond length (Å) to first O shell; N = coordination number; D.W. = Debye–Waller factor (disorder parameter; $Å^2$).

in framework sites. Fe foil was used to calibrate the position of the absorption edge.

Model compounds. Figures 2(a) and (b) show the expanded edge regions for five model compounds. Note that the pre-edge peak is much larger for 4-fold than for 6- and 8-fold coordination and that the edge crests show increasingly pronounced peaks in the order 4- to 6- to 8-fold coordination. The features of the feldspar (Madagascar orthoclase) spectrum in Fig. 2(b) show that Fe^{3+} is substituting for Al in the framework. Figure 2(c) shows expanded XANES spectra for crystalline "models" with Fe^{2+} in different types of 4-fold coordination: synthetic K–Fe leucite has Fe^{2+} in framework (network) sites replacing some of the Si atoms; staurolite has Fe^{2+} in large tetrahedral sites which form part of the spinel layer linked to octahedral Al; synthetic Fe-akermanite has Fe^{2+} in tetrahedral sites linked to SiO_4-dimers; and gillespite ($BaFeSi_4O_{10}$) has Fe^{2+} in square planar coordination. Note the distinctly different spectra which can be used as a fingerprint for the topology of the Fe-containing structural units. Table 2 gives refined EXAFS data for most of the model compounds. Bond lengths from X-ray crystal structure determinations are given in parentheses—agreement with EXAFS values is generally within 0.02 Å. As expected, Fe—O bond lengths show clear increases with coordination number. Note that the pre-edge peak height is significantly larger for 4-fold Fe, with that for Fe^{2+} being about half the intensity of that for Fe^{3+}. ΔE values clearly increase from Fe^{2+} to Fe^{3+}.

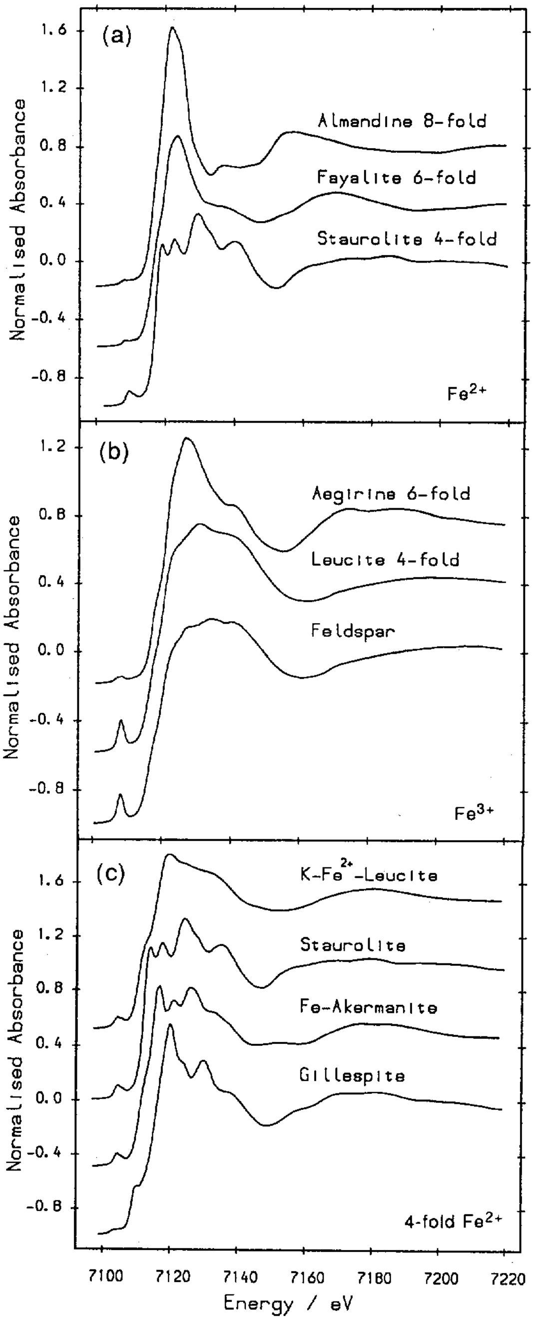

Fig. 2. Fe K-edge XANES spectra for: (a) Fe^{2+} crystalline model compounds with 8-fold (almandine, $Fe_3Al_2Si_3O_{12}$), 6-fold (fayalite, Fe_2SiO_4), and 4-fold (staurolite, see text) coordination; (b) Fe^{3+} model compounds with 6-fold (aegirine, $NaFeSi_2O_6$) and 4-fold ("leucite", $KFeSi_2O_6$) coordination and for feldspar (Madagascar orthoclase $KAlSi_3O_8$ with 2.6 wt% Fe_2O_3); (c) Fe^{2+} model compounds with different 4-coordinated Fe^{2+} geometries (Fe-akermanite, $Ca_2FeSi_2O_7$; gillespite, $BaFeSi_4O_{10}$).

The refined first shell distances can be combined with the equivalent crystallographic data for these and other minerals to assign typical 'standard' bond length values to both oxidation states in 4- and 6-fold coordination (denoted [4] and [6]):

$$Fe^{2+}[4]\ 1.98;\ Fe^{2+}[6]\ 2.12;$$

$$Fe^{3+}[4]\ 1.86;\ Fe^{3+}[6]\ 2.02\ \text{Å}.$$

Glasses. We have studied the Fe environments in some relatively simple alkali silicate systems, which have leucite-like stoichiometries, prepared at different oxygen fugacities. Samples prepared at latm. in air ($fO_2 = 10^{-0.68}$ atm.) have virtually fully oxidized Fe while those prepared at about $fO_2 = 10^{-10}$ atm. have an Fe^{2+}: Fe^{3+} of approx. 0.85:0.15. Other Na-rich glasses studied have similar oxidation ratios to these leucite glasses but Ca-rich glasses are relatively more reduced for the same synthesis oxygen fugacity. XANES spectra are shown in Fig. 3 and pre-edge peak heights given in Tables 3 and 4 along with refined EXAFS data.

XANES spectra for oxidized and reduced glassy forms of $Rb_2FeSi_5O_{12}$ are compared with the reduced crystalline "leucite" analogue in Fig. 3(a). The crystalline "leucite" has Fe^{2+} unambiguously in 4-coordinated network-forming sites. The oxidized glass spectrum is very similar to that of $KFe^{3+}Si_2O_6$ leucite [Fig. 2(b)] indicating that Fe^{3+} is 4-coordinated. The reduced K-Fe "leucite" glass has virtually the same spectrum as the crystal pointing to both glass and crystal having Fe^{2+} in essentially identical environments. Refined XAFS data confirm these assignments

Table 2. Refined first shell Fe data for crystalline model compounds

Valency	N	Sample	R	N Refined	D.W.	ΔE	P.E.	Cryst.
2+	4	K–Fe-leucite 1*	1.97	4.0	0.014	5.8	0.05	(?)
2+	4	Staurolite	1.99	3.2	0.015	7.8	0.07	(2.01)
2+	6	Hedenbergite	2.10	4.0	0.016	8.1	0.02	(2.13)
2+	6	Fayalite	2.09	4.9	0.026	8.0	0.03	(2.21)
2+	6	Ilmenite	2.06	4.5	0.027	8.9	—	(2.08)
2+	8	Almandine	2.21	9.2	0.041	8.9	0.02	(2.30)
3+	4	K–Fe-leucite 2*	1.85	3.8	0.008	10.1	0.12	(?)
3+	6	Aegirine	1.98	6.1	0.021	12.5	0.02	(2.01)
3+	6	Andradite	2.00	5.6	0.008	10.9	0.02	(2.02)
3+	3	Hematite	1.95	3.6	0.011	10.1	0.05	(1.95)
	3		2.13	1.6	0.006			(2.12)

R = bond length (Å) to first O shell (crystallographic values in parentheses); N = coordination number; D.W. = Debye–Waller factor (disorder parameter; Å^2); ΔE = separation between absorption edges for mineral and Fe foil (eV; Fe = 7115 eV); P.E. = pre-edge intensity relative to the step height.

*K-Fe-leucite 1 = $K_2Fe^{2+}Si_5O_{12}$; Fe-leucite 2 = $KFe^{3+}Si_2O_6$.

(Table 3) for a series of crystalline and/or glassy "leucites" having the stoichiometries: $XFe^{3+}Si_2O_6$ and $X_2Fe^{2+}Si_5O_{12}$, where X = Na, K, Rb and Cs. Irrespective of modifier cation, the pre-edge heights, coordination numbers and first shell distances are more consistent with both Fe oxidation states occupying 4-fold sites in the glasses. Note the distinctly different XANES for the glasses and crystalline leucites compared to those for other 4-fold coordinated Fe^{2+} compounds [cf. Figs 2(c) and 3(a)]. Furthermore, the close similarities of these data for a given composition glass to those for the equivalent crystalline phase (Table 3) together with the almost identical XANES [Figs 2(b) and 3(a)] suggest that

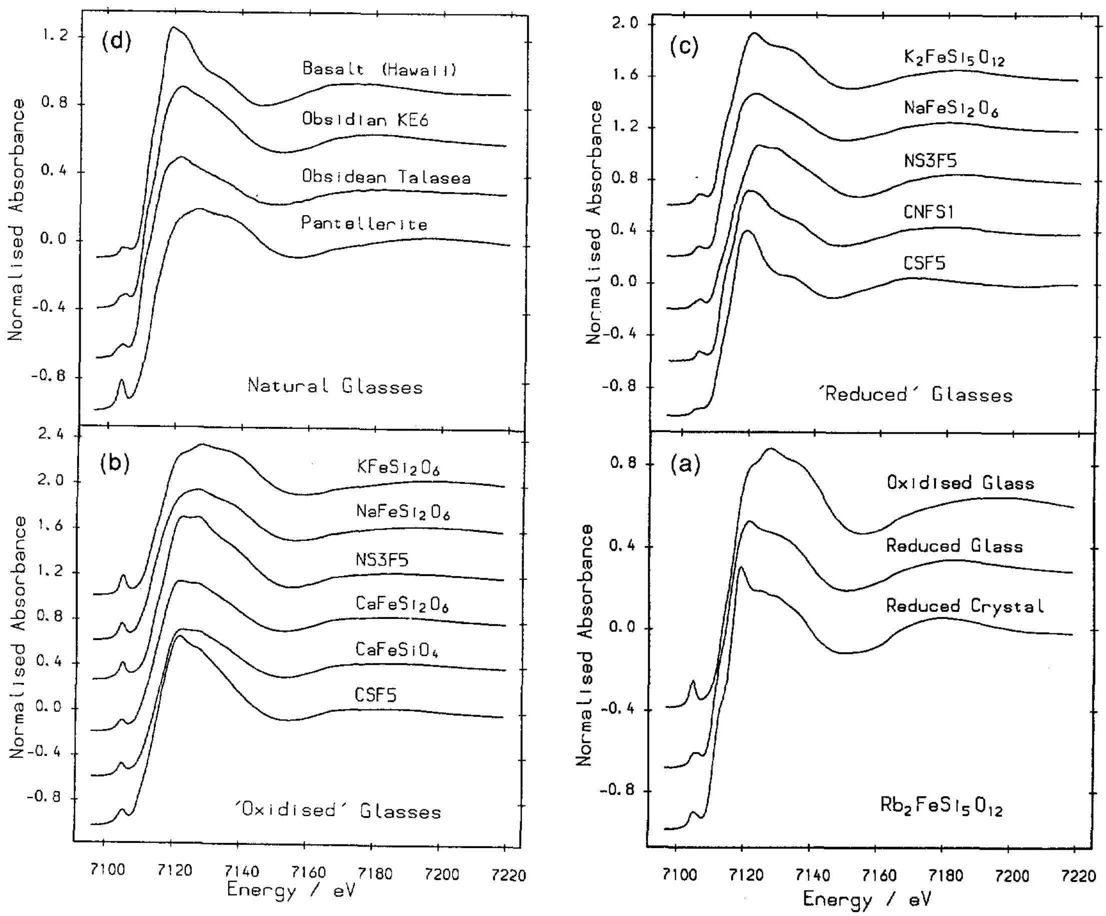

Fig. 3. Fe K-edge XANES spectra for: (a) reduced crystalline "leucite" analogue with $Rb_2FeSi_5O_{12}$ stoichiometry and for the equivalent reduced and oxidized glasses; (b) oxidized glasses (NS3F5 $Na_2O.3SiO_2$ + 5 wt% Fe_2O_3; CSF5 CaO · SiO_2 + 5 wt% Fe_2O_3); (c) reduced glasses (CNFS1 SiO_2 68.1, Al_2O_3 3.0, FeO 13.8, CaO 10.1, Na_2O 5.3 wt%); (d) natural basalt, obsidian and pantellerite glasses.

Table 3. Fe "leucite" crystal/glass first shell data

	N	*R*	*ΔE*	D.W.	P.E.
"*Standard*" *data*					
Fe^{3+}	4	1.86	10	0.008	0.12
	6	2.02	11	0.015	0.02
Fe^{3+}	4	1.98	6-7	0.015	0.06
	6	2.12	8	0.020	0.03
$XFe^{3+}Si_2O_6$ *(oxidized,* fO_2 10 $^{0.68}$ *atm)*					
K crystal	3.8	1.85	10.1	0.008	0.12
K glass	4.0	1.85	9.5	0.011	0.12
Na glass	4.0	1.86	10.1	0.015	0.11
$X_2Fe^{2+}Si_5O_{12}$ *(reduced,* fO_2 10^{-10} *atm)*					
K crystal	4.0	1.97	5.8	0.014	0.050
K glass	3.7	1.94	6.8	0.018	0.055
Na glass	3.6	1.96	6.3	0.019	0.060
Rb crystal	3.9	1.96	6.4	0.011	0.055
Rb glass	3.9	1.93	6.8	0.019	0.050
Cs crystal	3.8	1.98	7.3	0.018	0.040
Cs glass	3.5	1.95	6.8	0.018	0.060

N = coordination number; *R* = first shell distance to O, Å; Δ*E* = edge relative to Fe-metal, eV; D.W. = Debye–Waller factor, Å; P.E. = pre-edge height relative to edge step.

both Fe^{2+} and Fe^{3+} are present as network formers in the samples studied.

Figure 3b shows XANES spectra for other glasses prepared in air. The pre-edge and edge-crest features for $KFeSi_2O_6$ and $NaFeSi_2O_6$ glasses are characteristic of Fe^{3+} in 4-coordination (see above); NS3F5 has very similar XANES features but the first shell distance is rather long suggesting the presence of some octahedral Fe^{3+} (Table 4). $CaFeSi_2O_6$ and $CaFeSi_2O_4$ have rather smaller pre-edges and more-pronounced edge-crests and CSF5 is particularly noteworthy in the latter regard. The implication is that these Ca-bearing glasses, particularly CSF1, have significant amounts of octahedral Fe. First shell XAFS data support this conclusion (Table 4), indeed the low Δ*E* value for CSF5 indicates that the octahedral Fe is divalent. XANES features of reduced glasses [Fig. 3(c)] show similar variations. $K_2FeSi_5O_{12}$, $NaFeSi_2O_6$ and NS3F5 glasses appear to have XANES features and XAFS first shell data suggesting that Fe is dominantly in 4-coordination. Ca-bearing glasses CNFS1 and CSF5 have more pronounced edge-crest peaks suggestive of significant octahedral Fe being present and this assignment is supported by the longer first shell distances (Table 4).

Table 4. Refined first shell Fe data for glasses

Sample	*R*	*N*	D.W.	Δ*E*	P.E.
Oxidized glasses (prepared in air; $fO_2 = 10^{-0.68}$ *atm)*					
NS3F5	1.91	5.1	0.022	11.5	0.08
$CaFeSi_2O_6$	1.92	4.5	0.025	11.7	0.09
$CaFeSiO_4$	1.91	4.7	0.025	10.9	0.09
CSF5	1.92	3.8	0.017	6.8	0.05
Reduced glasses (fO_2 *of synthesis in parentheses, atm)*					
NS3F5 (10 ^{9})	1.96	5.1	0.026	6.8	0.05
CNFS1 (10^{-10})	1.99	3.8	0.022	6.7	0.05
CSF5 (10^{-9})	2.04	4.2	0.028	7.0	0.02
Natural rock glasses					
Basalt (Hawaii)	2.00	4.1	0.031	6.4	0.04
Obsidian (KE6)	1.92	3.7	0.025	6.6	0.05
(Talasea)	1.89	2.6	0.025	7.5	0.08
Pantellerite	1.86	2.5	0.007	9.8	0.15

R = bond length (Å) to first O shell; *N* = coordination number; D.W. = Debye–Waller factor; Δ*E* = separation between absorption edges for mineral and Fe foil; P.E. = pre-edge intensity relative to the step height.

Figure 3(d) shows XANES spectra for natural volcanic glasses and refined XAFS data are given in Table 4. The basalt glass spectrum is similar to that of crystalline fayalite [Fig. 2(a)] but the first shell distance is slightly short suggesting that although the Fe^{2+} in the glass is mainly in 6-fold, network modifier sites, some 4-coordinated Fe^{2+} may be present. The relatively reduced KE6 obsidian has a more-pronounced edge crest than the more-oxidized Talasea obsidian indicating that the former contains more octahedral Fe than the latter. The fully-oxidized pantellerite glass clearly has Fe dominantly in 4-coordination. The first shell distances increase from KE6 to Talasea to pantellerite consistent with these conclusions (Table 4).

Discussion. The conclusion that reduced $NaFeSi_2O_6$ glass has Fe mainly in four-coordinated network sites is at variance with predictions from Raman and Mössbauer studies (e.g. Virgo and Mysen, 1985) but is similar to those from XAS studies of both glasses and melts for alkali Fe silicate and fayalite compositions (Waychunas *et al.*, 1988; Jackson *et al.*, 1991). It seems that the quenched glasses are reliable models for Fe environments in the equivalent melts for these systems at least.

Dingwell and Virgo (1987) have measured the dependence of viscosities of melts of stoichiometry $NaFeSi_2O_6$ at 1430°C on oxygen fugacity. The decrease in viscosity from 23 P in air (Fe^{3+}/total Fe = 0.92) to 10 P at $fO_2 = 10^{-5.7}$ atm (Fe^{2+}/total Fe = 0.18) was correlated with the change from Fe^{3+} being present as a network former in the oxidized melt to Fe^{2+} being present as a network modifier in the reduced melts. Our results on oxidized and reduced $NaFeSi_2O_6$ (Table 3) point to both Fe^{2+} and Fe^{3+} being in network sites. We therefore account for the decrease in viscosity with increasing Fe^{2+} as reflecting the presence of longer, thus weaker, Fe^{2+}–O network bonds in the more reduced melts. It is noteworthy that $NaAlSi_2O_6$ melt at 1430°C has a viscosity of 1550 P, thus the decrease in viscosity on substitution of Fe^{3+} for Al in network sites demonstrates the effect of bond strength. Thus the reduced viscosity is not necessarily due to depolymerization of the network.

There also seems to be good evidence that Fe-bearing glasses having a variety of chemical compositions show the presence of significant amounts of Fe^{2+} in 4-fold coordination, most likely in network sites, suggesting that the network-former/network-modifier concept for silicate melt structures needs to be reconsidered.

Transition element structural environments in staurolite

The XAS technique has also been used to establish the sites occupied by minor elements in the chemically and structurally complex mineral staurolite (Henderson *et al.*, 1993) and vesuvianite (Ohkawa *et al.*, 1992). Staurolite is monoclinic (space group C2/m) with the idealized formula: $Fe_{3-4}Al_{18}Si_8O_{48}H_{2-4}$; minor amounts of Zn, Mn and Ti are ubiquitous. Smith's (1968) X-ray diffraction structure was refined on the basis of 7 octahedral and 2 tetrahedral cation sites. The chemical complexity and the presence of unfilled sites has led to many different cation assignment schemes. Most authors place Ti and Zn in the tetrahedral *T*2 site and Mn in the octahedral *M*4 sites, however, Stahl *et al.* (1988) assign Mn to *T*2, Ti to the distorted *M*2 site and divide Zn equally between *T*2 and *M*4 sites.

The element-specific nature of XAS and its ability to study minor components make it an ideal technique for elucidating this problem. We have studied the same sample as Stahl *et al.* (1988) to directly determine the environments of Mn (0.14 wt%), Zn (0.18%) and Ti (0.4%). Fluorescence detection methods were used to obtain spectra and the local structures were deduced from pre-edge (where present) and XANES features and refined XAFS parameters. Data from model compounds with Mn, Zn and Ti in either 6- or 4-fold coordination were used to constrain the structural assignments.

XANES features for Mn and Zn show distinct similarities to those for Fe (Fig. 4). Pre-edge height for Mn and refined XAFS parameters for Mn (first shell bond length to O = 2.01 Å) indicate that Mn is dominantly in 4-coordination. Note that significant structure out to 6 Å, similar to that for Fe, can be fitted to the Mn XAFS despite its much lower concentration. The Zn data are somewhat less clear. The XANES features and first-shell bond-distances (1.96 Å) both suggest 4-coordination but the refined coordination number and D.W. factor (both less reliable than bond distance data) are rather high. On balance, 4-coordination seems likely but the possibility that some Zn is in distorted 6-fold sites cannot be ignored. Refined XAFS first-shell, bond-distances (1.82 Å) together with XANES and pre-edge features (Fig. 5; cf. Waychunas, 1987), are consistent with Ti occupying distorted 6-fold sites, most likely the *M*2 sites.

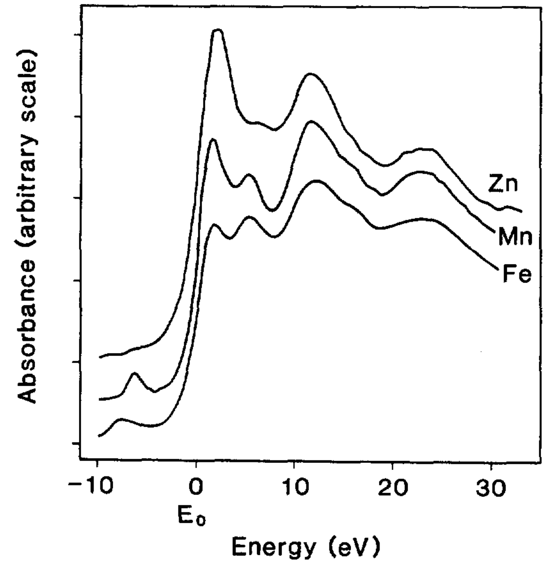

Fig. 4. XANES spectra for Fe, Mn and Zn K-edges in natural staurolite from Pizzo Forno (PF2), Switzerland.

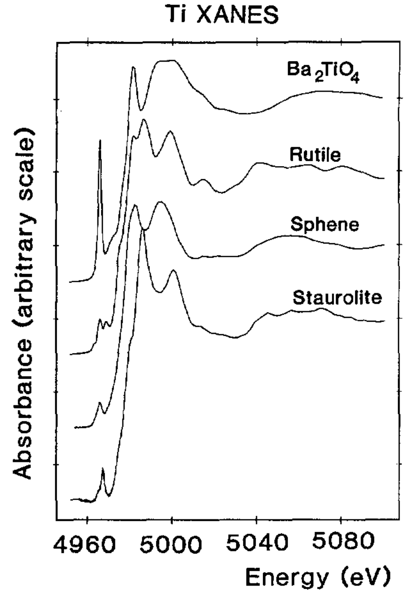

Fig. 5. XANES spectra for Ti K-edges in synthetic Ba_2TiO_4 (4-fold Ti), natural rutile (TiO_2) and sphene ($CaTiSiO_5$) (both 6-fold Ti), and natural staurolite (PF2).

Our assignments based on direct measurements for minor elements are closely similar to the crystal chemical assumptions of Stahl *et al.* (1988) showing the importance of the element-specific XAS technique for extending and testing diffraction data where scattering is dominated by major elements.

A 2p-XAS probe for multiple valency states of 3d transition elements

Until recently, most XAS work on 3*d* transition elements has been limited to studies of K-edges, but recent advances in instrumentation are now allowing $L_{2,3}$ edges to be explored. Unlike K-edges, the L absorption spectrum for 3*d* metals is dominated by dipole transitions from the core 2*p* level to empty 3*d* states. Because of the large Coulombic interaction between these two levels, the dipole transition energies and their occurrence probabilities depend on the local electronic structure. Thus analysis of the $L_{2,3}$ absorption structure provides information about the oxidation state(s), site symmetry, spin state, and crystal field splitting for 3*d* transition elements. Chen and Sette (1990), van der Laan and Kirkman (1992) and de Groot *et al.* (1992) have recently studied Ti environments in minerals by L-edge spectroscopy. Our group has recently exploited these new developments in a study of natural and synthetic minerals and glasses and much new, some of it unexpected, information was obtained (Cressey *et al.*, 1993). Interpretation of the spectra was greatly helped by using the atomic multiplet calculations of van der Laan and Kirkman (1992). Some of the principal results are summarized here.

Figure 6 shows Mn $2p$ absorption spectra representing $2p^5 3d^{n+1}$ transitions for a range of minerals containing Mn. The spectrum for rhodochrosite ($MnCO_3$) is characteristic of Mn^{2+} and corresponds almost exactly with the calculated spectrum for d^5 Mn in octahedral coordination with a crystal field splitting of about 1.0 eV (see van der Laan and Kirkman, 1992). The coexistence of Mn^{2+} and Mn^{3+} in the other minerals is expected from their crystal chemistry, and the presence of some pyrolusite (MnO_2) alteration products in vredenburgite and jacobsite accounts for the Mn^{4+}. Note that the different peak heights for the main Mn^{2+} and Mn^{3+} features gives invaluable information about the relative proportions of these oxidation states in the different minerals confirming that Cu^{1+} must be the dominant oxidation state in crednerite with subordinate Cu^{2+}.

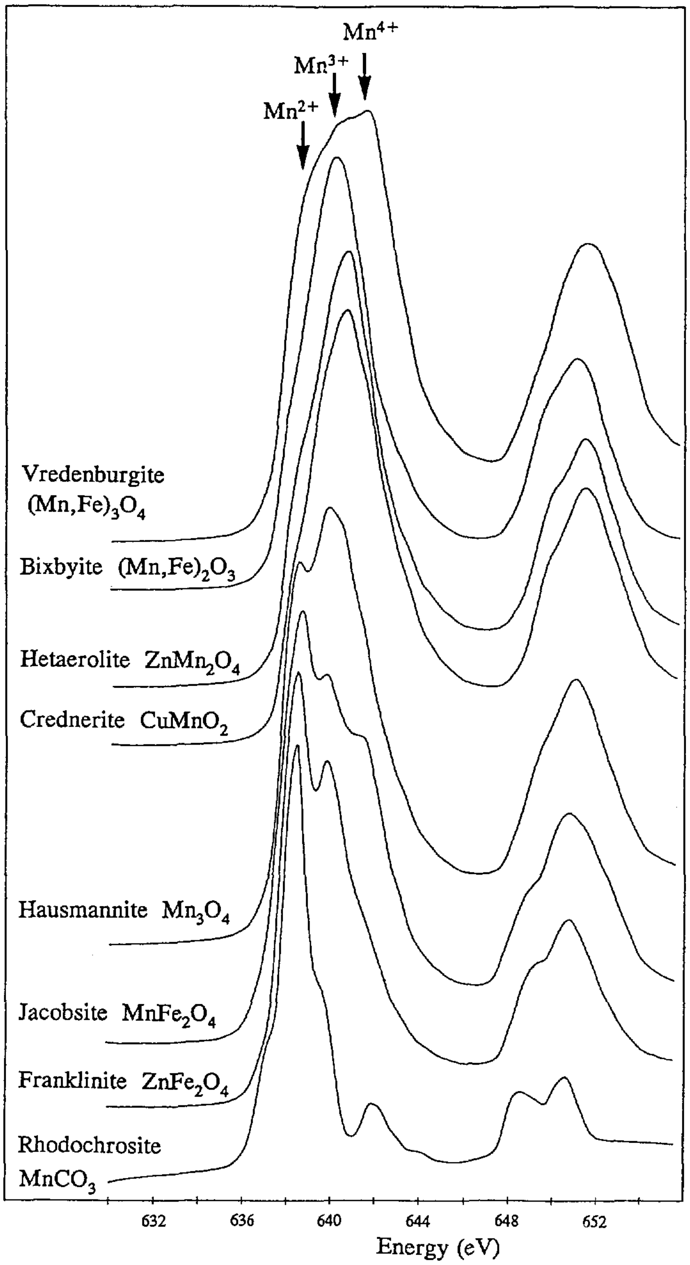

Fig. 6. L_3 and L_2 absorption spectra for a series of Mn minerals; relative energy positions of L_3 maxima shown at the top are based on calculations of van der Laan and Kirkman (1992).

We have attempted to quantify $Fe^{3+}/\Sigma Fe$ ratios for a range of single-phase, mixed-valent Fe-bearing minerals by comparison of experimental and theoretical spectra. Convoluted profiles, representing different oxidation ratios, are simulated by summation of the calculated multiplet structures of d^5 Fe^{3+} and d^6 Fe^{2+}, each with an appropriate site symmetry and $10D_q$. Note that the probability ratio for the $Fe^{3+}:Fe^{2+}$ transitions is 5:4, i.e. proportional to the numbers of d-holes. Figure 7 shows the results for a natural spinel: (a) is the experimental spectrum; (b) the simulated profile with experimental peak widths; and (c) shows the calculated multiplet structures for Fe $3d^5 \rightarrow 2p^5 3d^6$ (for both O_h and T_d) and Fe $3d^6 \rightarrow 2p^5 3d^7$ (for O_h), together with the summation of these peaks with machine resolution. Assuming spinel stoichiometry, the analytical $Fe^{3+}:\Sigma Fe$ ratio is 0.49 and this value is exactly matched by the L_3 peak simulation.

The technique is also applicable to dilute systems allowing study of natural amethyst quartz (α-SiO_2) which contains about 0.01% Fe. Previous studies of the factors controlling the colour of amethyst, by EPR and optical spectroscopy (e.g. Cox, 1976, 1977; Cohen, 1985), have led to the suggestion that iron is present as Fe^{4+} and Fe^{3+}. The $2p$ absorption spectrum for Fe in amethyst is shown in Fig. 8 and it is evident that d^4 Fe^{4+} cannot be identified, indeed the dominant oxidation state appears to be Fe^{2+}. The amethyst spectrum has been modelled by Fe^{2+} d^6 (T_d) with $10D_q = 1.0$ eV and Fe^{3+} d_5 (T_d) with $10D_q = 1.5$ eV, giving $Fe^{3+}/\Sigma Fe = 0.32$.

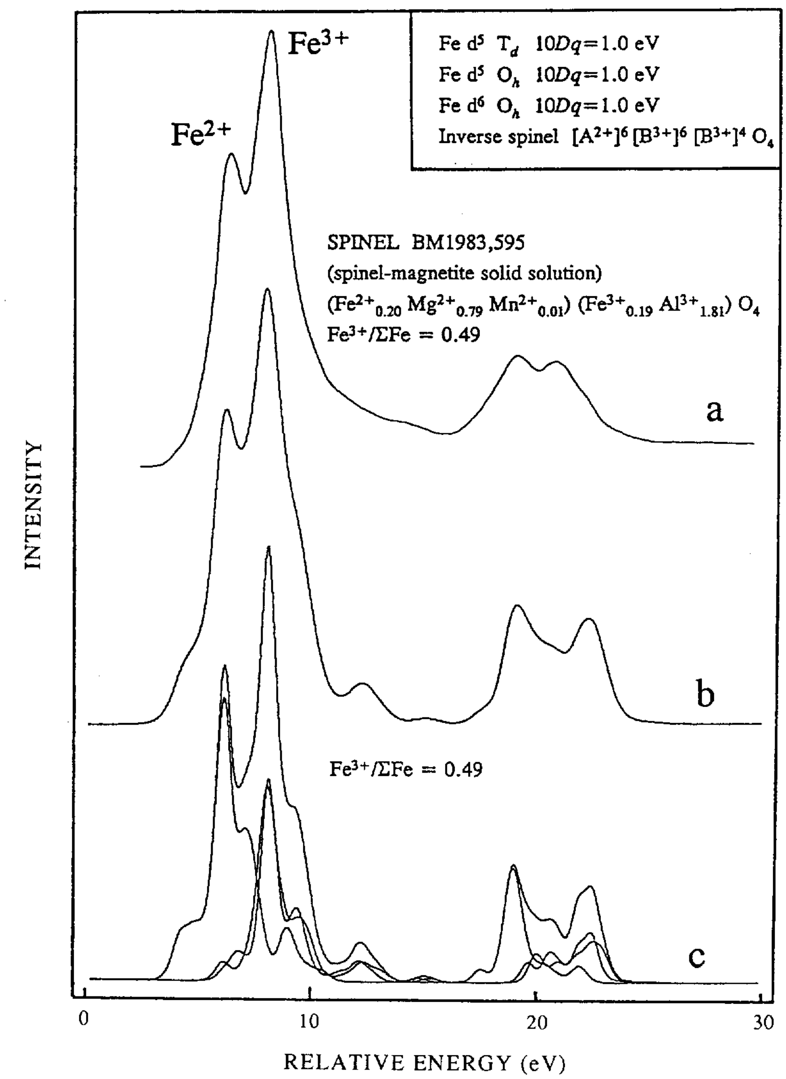

Fig. 7. Comparison of experimental and theoretical Fe L-edge spectra for a natural spinel: (a) experimental spectrum showing peaks assigned to Fe^{2+} and Fe^{3+} and the stoichiometry calculated from the electron microprobe analysis assuming 4 oxygens and 3 cations; (b) calculated spectra with broadened peaks; (c) convoluted profiles based on calculated spectra with machine resolution. See text for further explanation.

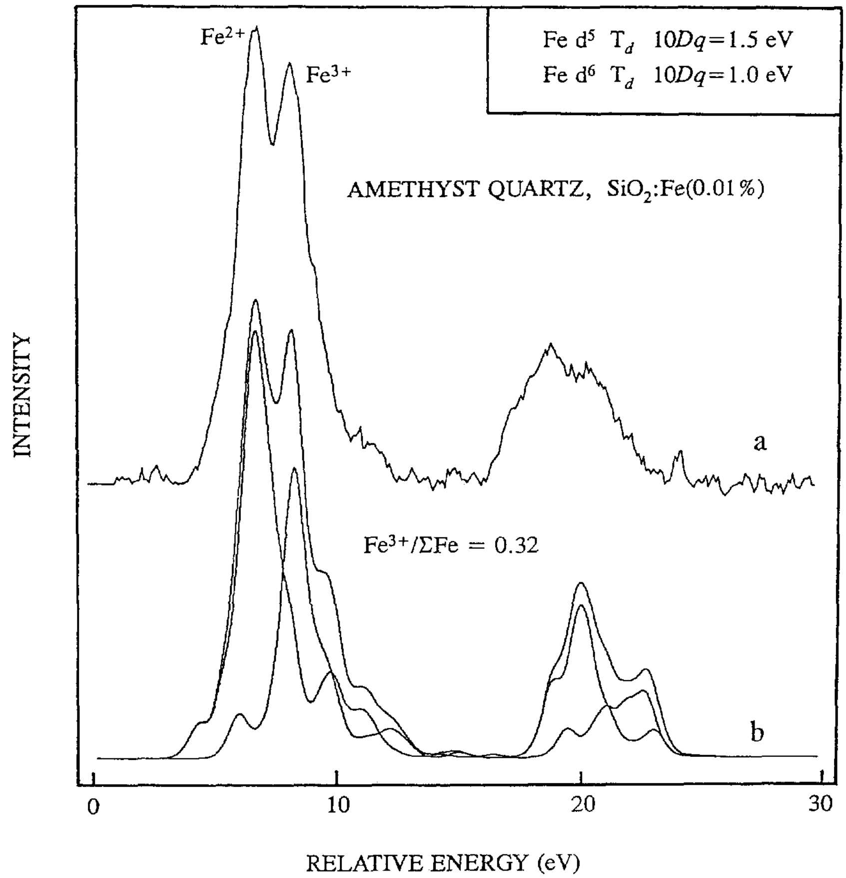

Fig. 8. Comparison of experimental and theoretical Fe L-edge spectra for natural amethyst quartz: (a) experimental spectrum; (b) best-fit simulation obtained from calculated spectra.

Single crystal polarized XANES

The polarization dependence of XANES in oriented single crystals can be studied effectively because of the nearly complete linear polarization of SR in its orbital plane. We have performed such experiments at the Fe K-edges for tourmaline, epidote and orthoclase, and at the Fe L-edges for gillespite, tourmaline, epidote and astrophyllite.

In tourmaline, Fe and Mg are accommodated in edge-sharing octahedral sites that form trigonal planar groups oriented perpendicular to the *c*-axis. The strong optical absorption pleochroism of this mineral is thought to be due to electron transfer between Fe^{2+} and Fe^{3+} electronic states in adjacent *A* sites (see Fig. 9). Figure 10 shows Fe K-edge single crystal XANES recorded in transmission mode using a 100 μm thick single-crystal section of tourmaline cut parallel to *c*. There is no obvious pre-edge peak consistent with the iron occurring as Fe^{2+} in comparatively symmetrical octahedral sites. The absorption anisotropy at and above the edge is clearly orientation-dependent. The main polarization-dependent feature is a shoulder on the edge that steadily becomes more prominent as the crystal is rotated towards the orientation with $E//c$. Polarization-dependent anisotropy in the XANES above the edge crest is also apparent. In contrast, a section cut perpendicular to the *c*-axis (optically isotropic) showed no X-ray absorption anisotropy for different azimuthal orientations, as would be expected. By comparison with Fe K-edges of other minerals (e.g. see Waychunas and Brown 1990), the edge feature that is most prominent when the electric vector is parallel to *c* is probably a 1*s*–4*p*-type bound state transition. The Fe site (site *A* in Fig. 9) in tourmaline has point symmetry *m*, so the *pz* orbitals will be normal to the mirror plane and thus oriented between the ligands, forming p_π hybrid molecular orbitals. Therefore, the $E \perp c$ spectrum will sample the 1*s*–4*pz* (p_π hybrid orbital) polarization. Depending on the orientation of the 4*px* and 4*py* orbitals within the mirror plane, the $E//c$ spectrum will sample one, or components of both, of these p_π-type orbital polarizations. For such an assignment, the spectrum with $E//c$ indicates that 1*s*–4*px*, *y* transitions occur with higher probability than the 1*s*–4*pz* transition.

The orientation-dependent anisotropy of the K-edge of Fe^{3+} in the *M*3 site in epidote is shown in Figs 11 and 12. Fe^{3+} is partitioned almost entirely into the *M*3 site; this has mirror symmetry, but is

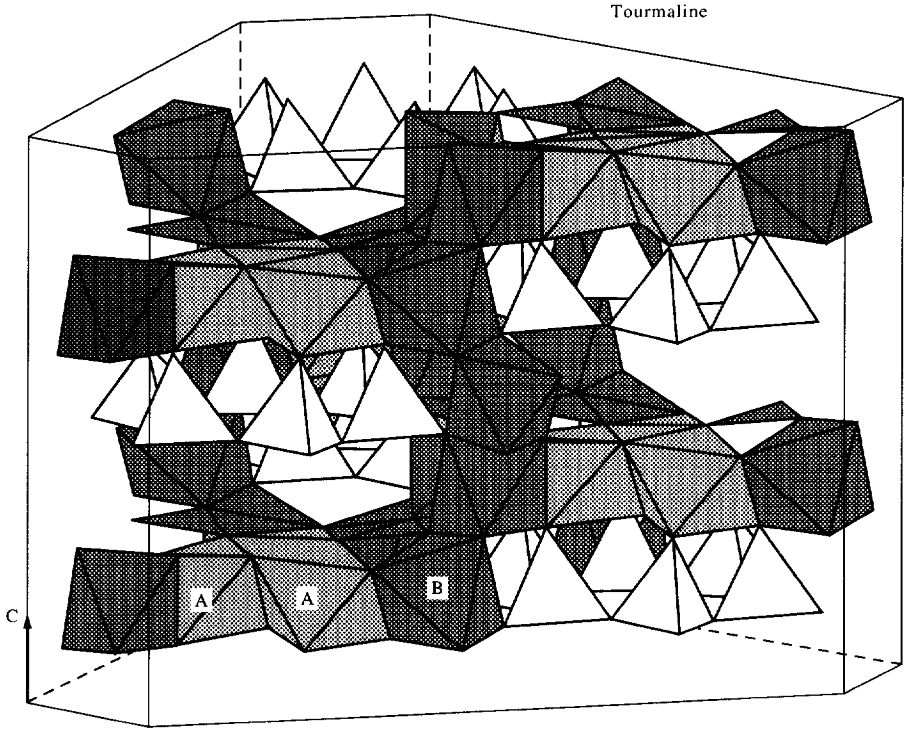

Fig. 9. The structure of tourmaline. Octahedral A-sites (Fe^{2+}, Mg), form edge-sharing trigonal-planar groups perpendicular to the *c*-axis. B-sites (mainly Al^{3+}) form spiral chains parallel to *c*.

non-centrosymmetric with irregular metal–oxygen distances. Because of the low crystal symmetry ($P2_1/m$), individual Fe—O bonds of the *M*3 site are directionally unique, and the absorption edge structure is sensitive to particular bond directions within this distorted site. The single-crystal polarized spectra shown in Figs 11 and 12 were recorded in fluorescence mode using a thick crystal slice cut parallel to (010), set at 45° to the incident beam and rotated about [010]; the different orientations of the *M*3 site

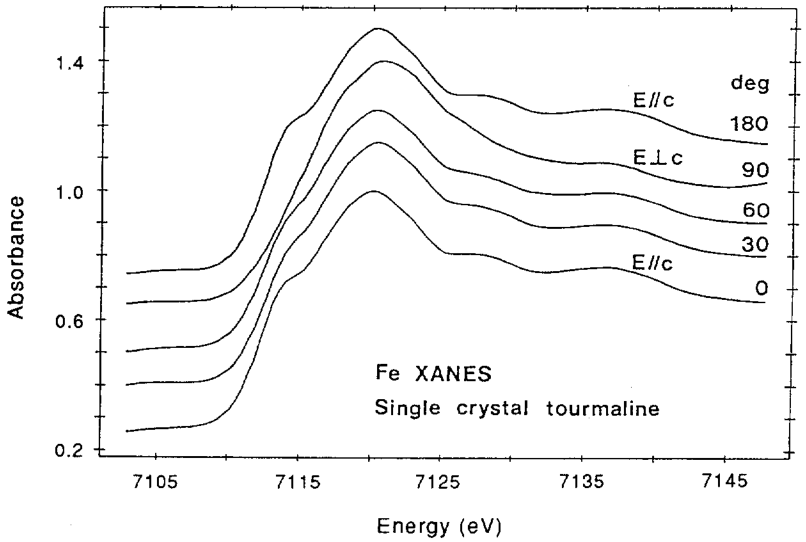

Fig. 10. Absorption anisotropy in Fe K-edge of single-crystal tourmaline, recorded in transmission geometry for different orientations.

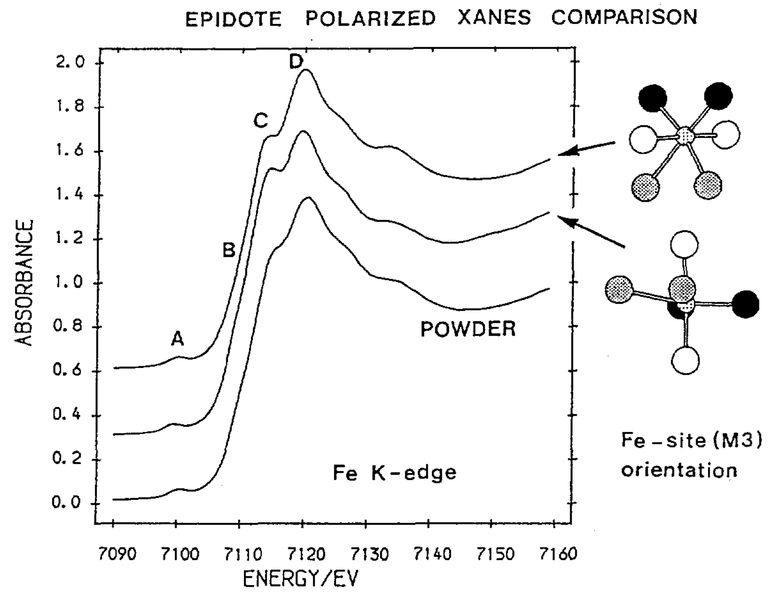

Fig. 11. Comparison of single-crystal polarized Fe K-edge XANES for different orientations of the *M*3 Fe-site in epidote, together with a spectrum of the powdered material.

relative to the horizontally plane-polarized incident radiation are shown by ball-and-spoke representations in the figures. The pre-edge peak size is typical of that for Fe^{3+} in distorted octahedral coordination. Four separate edge features are apparent; these are labelled (A), (B), (C) and (D) in Fig. 11. The pre-edge peak (A) is broad and consists of a doublet that can be assigned to $1s$–$3d(t_2g)$ and $1s$–$3d(e_g)$ transitions.

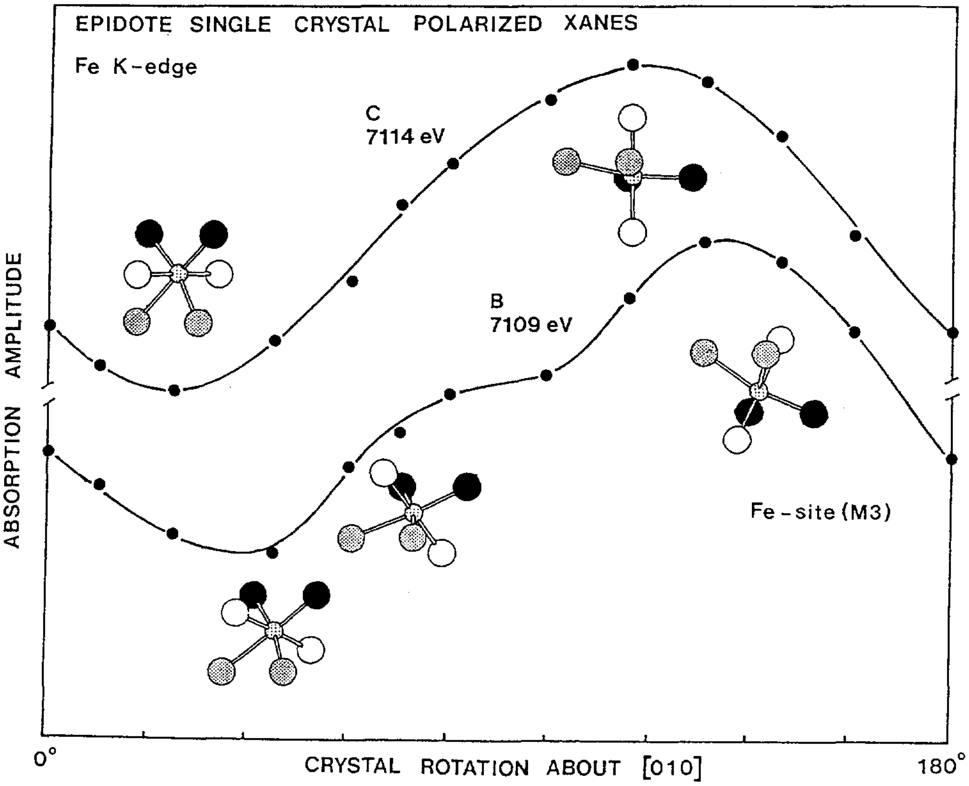

Fig. 12. The variation of absorption amplitude of edge features with the orientation of the *M*3 Fe-site in epidote.

The anisotropy in shoulder (B) with orientation is illustrated in Fig. 12, which shows that the probability of absorption corresponds with crystal orientations where the polarization plane of the incident radiation lies between the ligands. In this case, contributions from different $1s$–$4p_\pi$ type bound-state transitions are probably being sampled. At slightly higher energy, the feature labelled (C) may result from localized scattering resonance between absorber and backscattering atoms (see Waychunas and Brown, 1990) as the absorption maximum and minimum are associated with orientations where the Fe–O bonds are aligned with the incident polarization plane (see Fig. 12). The edge crest (D), has constant amplitude; this absorption isotropy is consistent with it representing a multiple-scattering-path resonance within the ligand cage of an electron excited to the continuum state.

In contrast to K-edges, L absorption spectra for $3d$ metals are dominated by dipole transitions from the core $2p$ level to empty $3d$ states. Therefore, polarized L-edge experiments can be performed which directly probe the final state orbital wavefunctions. Figure 13 shows polarized Fe $2p$ spectra for epidote, in which Fe^{3+} occurs in axially-compressed, non-centrosymmetric octahedra with site symmetry m. Spectra were recorded from a single crystal mounted with E parallel to the approximate square-plane (xy spectrum), and then with E parallel to the axial compression (z spectrum). The powdered (isotropic) spectrum is also shown. The energy range shown includes the Fe L_3 edge structure (high intensity peaks) and, at higher energy, the Fe L_2 edge (lower intensity peaks). Components of t_2g and e_g orbitals are present in both the xy (in-plane) and z (out-of-plane) spectra. However, the xy spectrum is dominated by $e_g(dx^2-y^2)$ and $t_2g(dxy)$ final states, with components of $t_2g(dxz, dyz)$ represented by the shoulder on the low energy side of the L_3 structure. The z spectrum is dominated by the $e_g(dz^2)$ final state, with components of t_2g (dxz, dyz) represented by the peak on the low energy side of L_3. The $e_g(dz^2)$ state has the highest energy, as expected for an axially-compressed octahedral environment. The L_3 structure for the powdered spectrum has t_2g (lower energy) and e_g (higher energy) spectral parts.

Structure of synthetic $K_2MgSi_5O_{12}$-leucites by X-ray powder diffraction

The natural mineral leucite ($KAlSi_2O_6$) has a 3-D framework of linked silicate and aluminate tetrahedra with channels occupied by potassium ions. During cooling from elevated temperatures, leucite undergoes a displacive phase transition from cubic to tetragonal symmetry. This transition can be simply regarded as a displacive collapse of the tetrahedral framework about the large K-cation but some workers have suggested that Al–Si ordering could play a significant role. As part of a wider attempt to understand the controls and consequences of tetrahedral-cation ordering in leucites, our research group is studying a series of synthetic "leucite" analogues of general formula: $X_2^+Y^{2+}Si_5O_{12}$, related to leucite (s.s.) by the coupled framework cation substitution 2Al = Mg,Si (Torres-Martinez and West, 1989). It transpires that such compounds are more amenable to T-site analysis than Al–Si analogues, and also display significant response to T-site ordering.

We will focus here on samples having the stoichiometry $K_2MgSi_5O_{12}$. In a magic angle spinning NMR study, Kohn *et al.* (1991) showed that dry-synthesized (800°C, 1 atm) $K_2MgSi_5O_{12}$ leucite has a disordered arrangement of T cations, while a hydrothermally synthesized sample (600°C, 500 bars water vapour pressure) has an ordered arrangement of Si and Mg on tetrahedral sites. The principal results of structure determination by Rietveld refinement (Rietveld, 1969) of synchrotron X-ray powder data from these two types of $K_2MgSi_5O_{12}$ (Bell *et al.*, 1995; in press) are summarized here.

Dry-synthesized sample. From the systematic absences in the powder pattern, the dry-synthesized

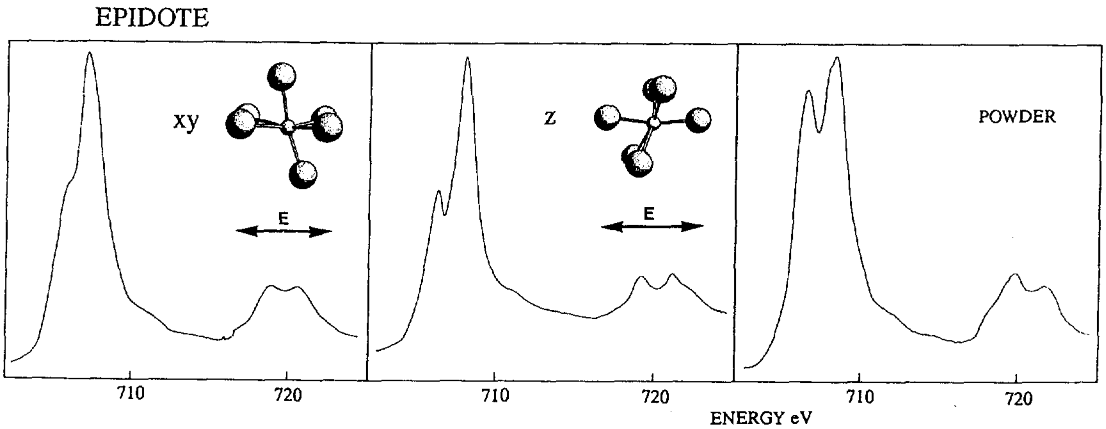

Fig. 13. Polarized $2p$ X-ray absorption spectra for different orientations of the $M3$ Fe-site in epidote, together with a spectrum of the powdered material.

sample was found to be body-centred cubic ($a = 13.4190(1)$ Å), space group $Ia3d$, and thus is similar to the metrically cubic, high-temperature polymorph of natural leucite (Peacor, 1968). The high-temperature single-crystal structure of natural leucite was therefore used as a starting point to refine the dry $K_2MgSi_5O_{12}$ structure, with Mg + Si replacing 2Al and assuming that all 48 T sites are disordered.

Hydrothermally synthesized sample. The superimposed diffraction patterns of the dry and hydrothermally synthesized samples are shown in Fig. 14. Clear similarities are apparent between the two patterns as groups of Bragg reflections in the hydrothermal sample coincide with individual reflections in the dry, cubic sample. These similarities are consistent with both samples having the same framework topology. In addition, closely similar cell volumes suggest that both unit cells have the same contents. It was found that the cubic coordinates could all be related by the symmetry operations for the $P2_1/c$ space group. In the $P2_1/c$ cell, the only Wyckoff position that could accommodate any of the atoms is the general position. To accommodate 48 T atoms, 12 different 4e positions are required which confirms the deduction from the NMR results of 12 T-sites (10Si and 2Mg; Kohn *et al.*, 1991). This fully ordered framework structure thus contains 4 distinct K-, 10Si- and 2Mg-sites per 24 oxygens (one quarter of the unit cell). The final unit cell parameters from the Rietveld refinement are: $a = 13.168(5)$, $b = 13.652(1)$, $c = 13.072(5)$ Å, $\beta = 91.69(5)°$.

During the refinement, two T–O distances were clearly longer than the others; these T sites were assigned to the two Mg atoms. The final refinement gave mean values of 1.92 and 1.88 Å for Mg–O while the other 10 mean distances (Si-O) were in the range 1.59–1.65 Å. From the determined tetrahedral connectivities it can be seen that two Si sites are only linked to next-nearest-neighbour (NNN) silicons. These T-sites are Q^4(4Si) sites [note use of NMR terminology which denotes a tetrahedral cation species (Q) linked to 4 NNN Si atoms]; all other Si sites are linked to one Mg NNN-atom (i.e. Q^4(3Si,1Mg)). The tetrahedral Q^4(4Si) and Mg(4Si) sites occupy opposite corners of four rings. The structures of the disordered, dry-synthesized leucite and the fully-ordered, hydrothermally-crystallized sample are shown in Fig. 15 with the three different T-site species in the latter phase identified with different shadings.

Discussion. The disordered form of $K_2MgSi_5O_{12}$-leucite has a distinctly larger unit cell volume than the ordered form (2416 and 2348 Å^3, respectively). Thus the ordering of the Si and Mg tetrahedral cations is accompanied by a contraction of 2.8%. The mean T–O–T angles for the two forms are 144.5° and 137.4° showing that the ordered sample is in a significantly

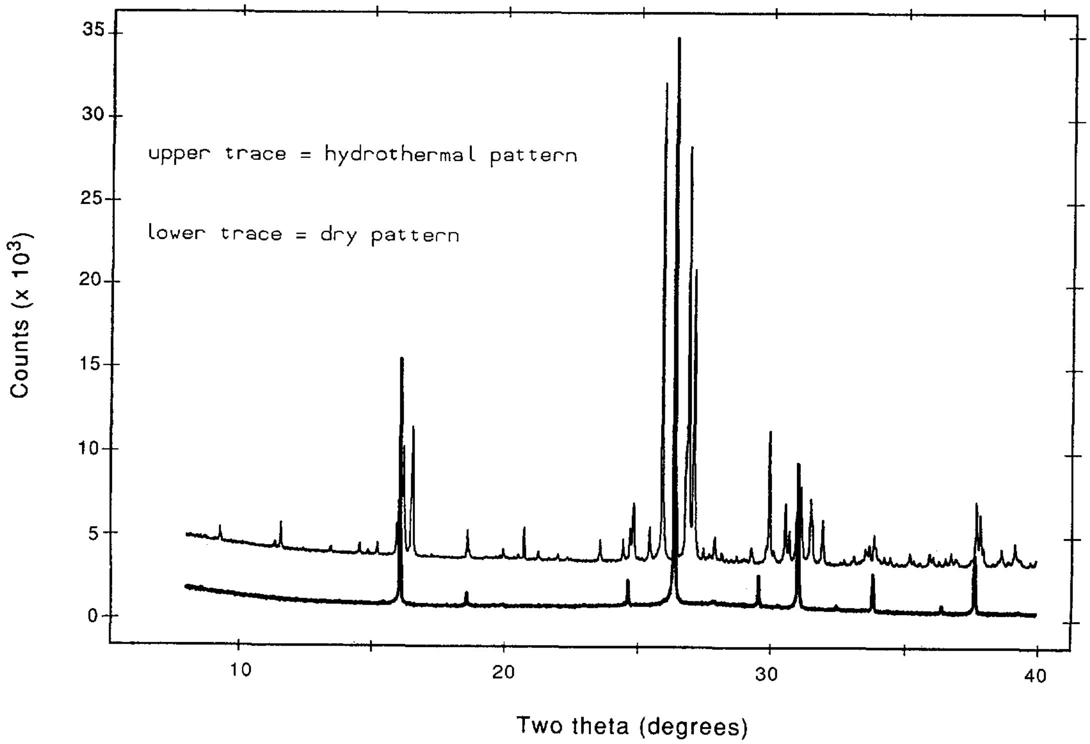

Fig. 14. Superimposed synchrotron powder diffraction patterns for dry- and hydrothermally-synthesized $K_2MgSi_5O_{12}$ leucites. Note how the latter sample has groups of peaks in the vicinities of single peaks in the cubic dry-synthesized sample.

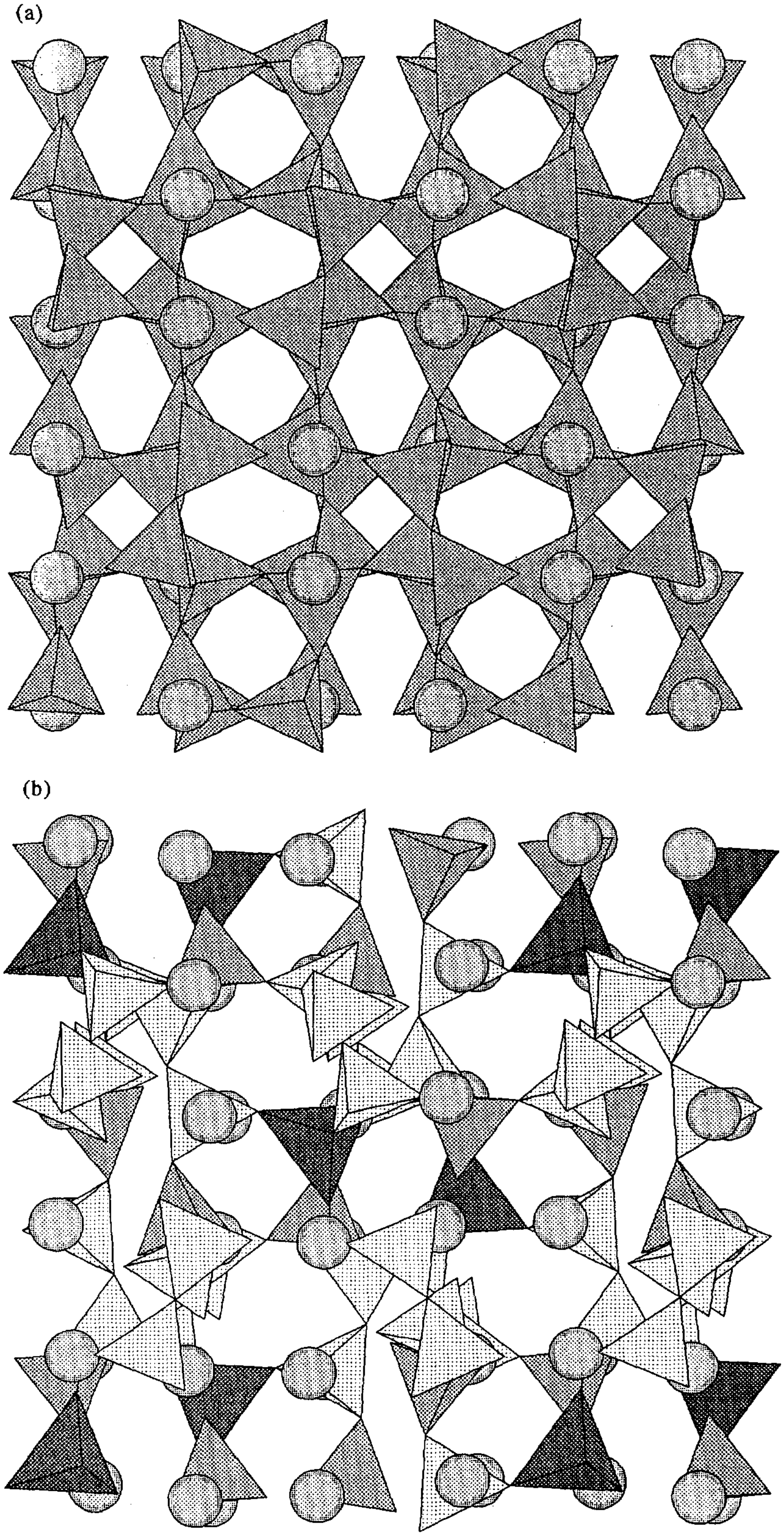

Fig. 15. (a) Cubic structure of dry-synthesized $K_2MgSi_5O_{12}$ leucite; projection on (100); (b) structure of hydrothermally-synthesized $K_2MgSi_5O_{12}$ leucite, projection on (100). Dark shaded tetrahedra represent Mg-sites, medium shaded are Q^4(4Si) and light shaded are Q^4(3Si,1Mg) tetrahedra.

more collapsed state. In the ordered structure the increase in the T–O bond lengths from Si–O (1.61 Å) to Mg–O (1.9 Å) is accompanied by a decrease in T–O–T bond angles from a mean of 141° for Si–O–Si to a mean of 131° for Si–O–Mg; it seems that the smaller Si–O–Mg angles are directly related to the increased framework collapse in the ordered structure. Indeed, the higher angular variance of the Mg tetrahedra relative to Si tetrahedra (40.4 and 20.9$^{\circ 2}$, respectively) points to the structural flexibility of the Mg–O_4 tetrahedra in the framework.

We have shown that the hydrothermally-synthesized $K_2MgSi_5O_{12}$-leucite has a crystal structure derived from that for the dry-synthesized cubic polymorph. Ignoring T-site ordering, the two structures are topologically identical, however the polymorphism is directly related to the T-site ordering which occurs during hydrothermal synthesis. It seems that the charge and size of Mg^{2+} (as opposed to Al^{3+}) are sufficiently distinct from those of Si^{4+} to ensure that the fully-ordered, thermodynamically more-stable, monoclinic form is formed relatively rapidly due to the catalytic action of water in the hydrothermal synthesis. The existence of the ordered and disordered forms of $K_2MgSi_5O_{12}$ leucite thus reflects the distinctly different kinetics of the two synthesis techniques employed and, in this case, is not related to a high–low-temperature reversible phase transition.

The connectivity information deduced from the NMR spectra (Kohn *et al.*, 1991) and determined in the present work for the ordered sample, shows that the Mg tetrahedra are separated by two Si tetrahedra and that the Q^4(4Si) species are also separated by two Q^4(3Si,1Mg) Si tetrahedra. Thus it seems that the energetic disadvantage of Si–O–Mg–O–Mg–O–Si and Si–O–Mg–O–Si–O–Mg–O–Si arrangements within the framework structure is significantly greater than that recognized in aluminosilicates as Al-avoidance (Dempsey *et al.*, 1969; Loewenstein, 1954). The monoclinic, ordered structure which our refinement has yielded does indeed satisfy this principle as Mg. . .Mg distances are maximized.

Kohn *et al.* (1991) showed that the two NMR peaks occurring at chemical shifts of −91.0 and −104.5 ppm (relative to TMS) resulted from Q^4(4Si) units. They pointed out that the very small shift of −91.0 must correspond to an exceptionally small mean Si–O–Si angle. We can now assign a value of 134.9° to this peak and a Si–O–Si angle of 146.8° for the NMR peak at 104.5 ppm. Dupree *et al.* (1992) have used these data to assess the reliability of published correlations between ^{29}Si chemical shifts for Q^4(4Si) units and structural parameters, the principal conclusions being that the linear correlation between chemical shift and mean T–O–T angle cannot be used at small T–O–T angles, and that when a particular site has a wide distribution of Si–O distances and Si–O–T angles the correlation may break down. In addition, an empirical correlation between chemical shift and mean T–O–T angles for Q^4(3Si,1Mg) silicons was deduced.

High-pressure powder diffraction of gillespite ($BaFeSi_4O_{10}$)

The unique characteristics of SR make it particularly suitable for ED diffraction (EDD) of samples held at pressure in the diamond anvil cell. Powder diffraction of Earth materials becomes feasible, and phenomena such as structural phase transitions may be studied, not only at temperatures corresponding to the Earth's interior, but also in the high-P regime. We have demonstrated the utility of the EDD technique to mineralogical problems of this type in a study of the tetragonal (P4/ncc) to orthorhombic ($P2_12_12_1$) phase transition in gillespite (Redfern *et al.*, 1993). This transition has attracted attention in the past because the square planar coordinated Fe^{2+} in tetragonal gillespite changes to distorted tetrahedral coordination in the orthorhombic phase. A startling reversible colour change from red (tetragonal) to blue (orthorhombic) accompanies the transition, which was first investigated by optical absorption and Mössbauer spectroscopy (Huggins *et al.*, 1976; Abu-Eid *et al.*, 1973).

Gillespite is a layer silicate and the reversible transition results in rotations of SiO_4 groups and changes in Ba coordination (Hazen and Burnham, 1974; Hazen and Finger, 1983). The transition must induce a ferroelastic strain (since it corresponds to a reduction in crystal system), and it is this strain which we set out to measure by EDD at the Wiggler beam line 9 at the Daresbury SRS. In these experiments, ruby fluorescence was used to measure pressure.

Cell parameters were refined (Fig. 16), the transition being observed at $P_{Tr} = 1.2 \pm 0.1$ GPa. Peak splitting of orthorhombic peaks increases up to 4.3 GPa, the upper limit of our experiments. The transition not only shows splitting of the tetragonal *a* parameter into orthorhombic *a* and *b* parameters, but also an anomalous compressibility along *c*. The lattice parameter data reflect the onset of both ferroelastic and non-ferroelastic spontaneous strains above P_{Tr}. The ferroelastic strain (e_s) corresponds to the splitting of *a* and *b* and is proportional to $(a-b)/(a+b)$. The co-elastic strain (e_{vol}) corresponds to the jump in the trend of $1/2(a+b)$ and *c* in the orthorhombic phase compared with the values expected (in the absence of a transition) by extrapolation of the tetragonal data to high P.

Discussion. The results demonstrate that the transition in gillespite is not simply a ferroelastic shear, but also incorporates a volume contraction resulting from the coelastic strain. This high-P behaviour can be rationalized according to a Landau-type model in which the driving free energy for the transition is P-dependent and can be described by two order parameters Q_1 (proportional to e_s) and Q_2 (proportional to $(e_{vol})^{-1/2}$). The former corresponds to the change in crystal system and the latter to the

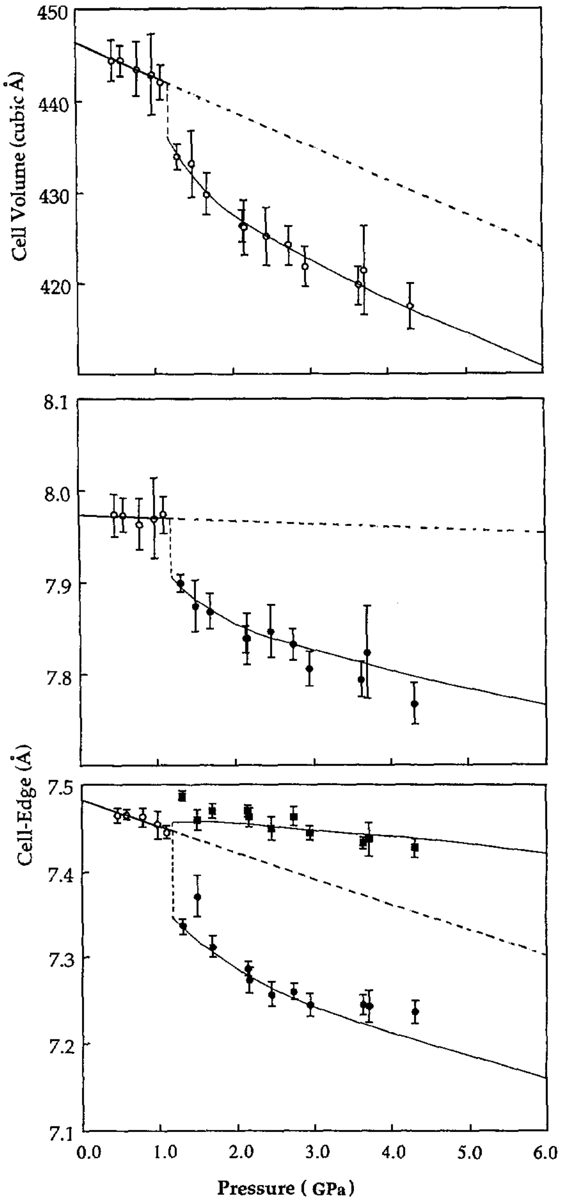

Fig. 16. Cell parameters of gillespite as a function of pressure. Solid lines serve to guide the eye, dashed lines indicate the linear extrapolation of the low-P high-symmetry cell into the orthorhombic field.

additional symmetry changes which does not involve a crystal system change. Since the orthorhombic space group $P2_12_12_1$ is not a maximal subgroup of P4/ncc this second order parameter may be associated with an intermediate structure necessary to complete the high-P transformation. This is seen in Fig. 17 where possible intermediate space groups are suggested. The ferroelastic process (Q_1) is shown by heavy arrows and the coelastic process (Q_2) by light arrows. The high-P experiments show that both these order parameters display first-order behaviour, with a jump at P_{Tr}.

The excess free energy in the orthorhombic phase is given according to the Landau model as:

$$\Delta G = 1/2AQ_1^2 + 1/4BQ_1^4 + 1/6CQ_1^6 + \xi Q_1^2Q_2 + 1/2\alpha Q_2^2 + 1/4\beta Q_2^4 + 1/6\gamma Q_2^6 \ldots$$

where A and α are linearly pressure-dependent parameters and ξ is the coupling constant linking Q_1 and Q_2. The physical process corresponding to ξ will be a lattice strain. Stability is determined by minimization of ΔG with respect to Q_1 and Q_2:

$$\delta\Delta G/\delta Q_1 = Q_1(A + 2\xi Q_2 + BQ_1^2) = 0$$

$$\delta\Delta G/\delta Q_2 = Q_2(\alpha + \beta Q_2^2) + \xi Q_1^2 = 0$$

which has three possible solutions:

(I) $Q_1 = Q_2 = 0$: the low-P tetragonal phase
(II) $Q_1 = 0$, $Q_2 \neq 0$,
(III) $Q_1 \neq 0$, $Q_2 \neq 0$: the high-P orthorhombic phase.

Phases I and III have point groups 4/mmm and 222. Phase II is an intermediate, which (from Fig. 17) can only correspond to point group $\bar{4}2$m or 422. We have no evidence for the existence of this intermediate as a discrete phase, although it could occur over a very limited P range near P_{Tr} (rather like the incommensurate phase of quartz at the α–β transition). It remains possible that the transition progresses as I → II on increasing pressure, rather than I → II → III, and we favour the first of these pathways in the light of our data.

Compressibility of $MgCO_3$ and its stability in the Earth's lower mantle

Carbonates are likely to be the main hosts of carbon in the Earth's mantle and both magnesite

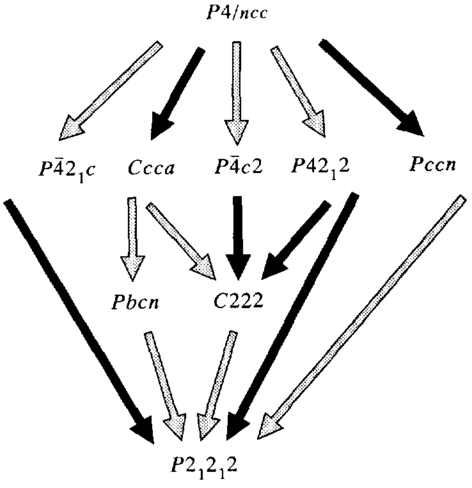

Fig. 17. Space group relations between the low-P P4/ncc space group of gillespite I and the low symmetry $P2_12_12_1$ space group of gillespite II. $P2_12_12_1$ is not a maximal subgroup of P4/ncc, and transitions via maximal subgroups may take place via ferroelastic (heavy arrows) and coelastic (light arrows) transitions.

($MgCO_3$) and dolomite ($CaMg(CO_3)_2$) have been described as inclusions in mantle-derived pyrope garnet (McGetchin and Besancon, 1973). Experimental work has shown that magnesite is the only stable carbonate in peridotite at pressures above 3.5 GPa. In order to assess whether magnesite might be the stable carbonate in the lower mantle, members of our research group have determined its compressibility up to 20 GPa using ED powder XRD (Redfern *et al.*, 1993). A natural magnesite sample was loaded into a diamond anvil cell and its cell parameters determined using the "white" beam, Wiggler station 9.7 at the SRS.

The axial and volume compressibilities (a/a_0, c/c_0, and V/V_0) are shown as a function of pressure in Fig. 18; the cell-parameters at up to 20 GPa show no discontinuities suggestive of a phase transition. The c/a ratio decreases from 3.235 at RTP to 3.104 at 20 GPa. This degree of anisotropy is a general feature of rhombohedral carbonates as similar results have been found for ankerite ($FeCO_3$) and dolomite (Ross and Reeder, 1992). This anisotropy results from the lower compressibility of CO_3 groups, which are parallel to the *x–y* plane, compared to that of MgO_6 octahedra.

The mean volume compressibility of $5.98 \times 10^{-3}\,GPa^{-1}$ corresponds to a mean bulk modulus of 167 GPa. However, the cell volume does not vary linearly with pressure so the isothermal bulk modulus (K_T) is not constant. Depending on the method of data analysis, values obtained for K_T and its pressure derivative (K'_T) vary from 142–151 GPa and 5.0–2.5, respectively. Assuming that the high-temperature stability limit for magnesite is the decarbonation reaction: $MgCO_3 = MgO + CO_2$, the bulk modulus data were combined with necessary thermodynamic parameters to calculate the P–T stability curves shown in Fig. 19. Thus, magnesite should be stable at least up to the solidus of rocks having peridotite or pyroxenite chemistry, and is likely to be a stable host for carbon in the lower mantle.

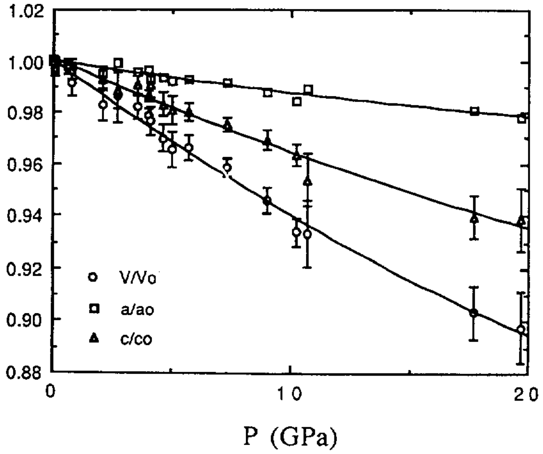

Fig. 18. Variation of a/a_0, c/c_0 and V/V_0 as a function of pressure; parameters with subscript "o" refer to values at 1 bar. Error bars indicate ± 1σ.

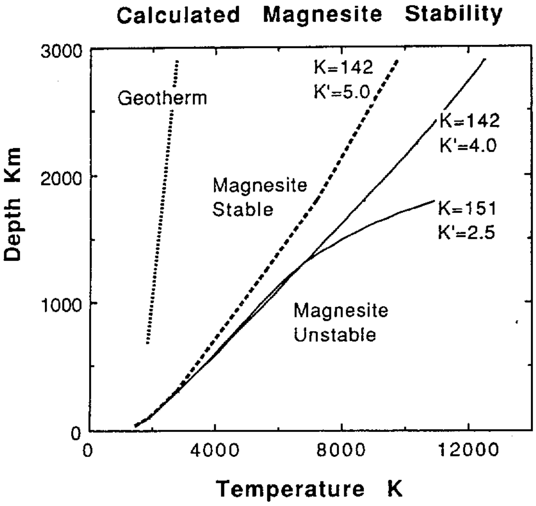

Fig. 19. Calculated stability of magnesite ($MgCO_3 = MgO + CO_2$). For the bulk modulus values calculated here, magnesite is seen to be stable to temperatures more than 2000 K above the lower mantle geotherm.

CLOSING REMARKS

The topics summarized above cover a reasonably wide range of recently completed and developing Earth sciences research at Daresbury. In the XAS area we believe that the "conventional" XAFS approach will greatly benefit from, for first row transition elements at least, the application of L-edge spectroscopy to determining local electronic structures. In particular, element-specific polarized L-edge experiments with single crystals provide direct information about site symmetries and the orientations and energies of 3d metal orbitals involved in bound-state transitions. Furthermore, such spectra also hold valuable information on the magnitude of the crystal field and its effect on different ionic configurations. Developments of high-temperature cells for studying metals in aqueous electrolyte solutions at up to 350°C are starting to provide new information on metal complexing of interest to geochemists and materials scientists.

In-situ XRD experiments at elevated pressures and/or temperatures will also provide much fundamental information on phase transitions and "equation of state" data of interest to mineralogists, petrologists and geophysicists. Development of "on-line", large-volume, multi-anvil presses allowing simultaneous P–T conditions up to 25 GPa and 2000 K will be particularly important. Indeed, it is anticipated that current developments will rapidly allow the extension of Rietveld powder structure determinations to the study of Earth materials at these extreme P–T conditions. The diamond-anvil cell, ED powder diffraction experiments discussed above have shown that, despite the limitations in structural information and resolution (compared with single crystal and angle dispersive diffraction) available, this relatively simple and rapid technique can yield important insights into mineral behaviour at high pressures. Further studies of displacive-type transitions at high-P should lead to a better understanding of relevant transition mechanisms as well as testing the applicability of Landau-related models in the high-P regime.

Acknowledgements—We thank Tony Bell and John Charnock for their invaluable assistance with the XRD and XAS research programmes, respectively. We also acknowledge the SERC for beam-time allocations via the Minor Grant scheme, the NERC for provision of research grant GR3/6653, and the Earth Sciences Directorate of NERC for a special grant supporting XAS data reduction. Constructive comments by an anonymous referee are also acknowledged.

REFERENCES

Abu-Eid R., Mao H. K. and Burns R. G. (1973) *Carnegie Inst. Washington, Year b.* **72,** 564–567.

Andrault D. and Poirier J. P. (1991) *Phys. Chem. Miner.* **18,** 91–105.

Andrault D., Madon M., Itié J. P. and Fontaine A. (1992) *Phys. Chem. Miner.* **18,** 506–513.

Andrault D., Peyronneau J., Petit P. E. and Itié J. P. (1993) *Terra Abs.*, (Suppl. 1) *Terra Nova* **5,** 361.

Artioli G. and Kvick Å. (1990) *Eur. J. Miner.* **2,** 749–759.

Behrens P., Abmann S., Felsche J., Vetter S., Schulz-Ekloff G., Jaeger N. I. and Niemann W. (1991) In *X-ray Absorption Fine Structure, Proc. VIth International XAFS Conference* (Edited by Hasnain S. S.) pp. 552–555. Ellis-Horwood, Chichester.

Binsted N., Greaves G. N. and Henderson C. M. B. (1985) *Contrib. Mineral. Petrol.* **89,** 103–109.

Binsted N., Greaves G. N. and Henderson C. M. B. (1986) *J. Phys. C*8, **47,** 837–840.

Bell A. M. T., Henderson C. M. B., Redfern S. A. T., Cernik R. J., Champness P. E., Fitch A. N. and Kohn S. C. (1995) *Acta Crystallogr. B*, In press.

Bidoglio G., Gibson P. N., O'Gorman M. and Roberts K. J. (1993) *Geochim. Cosmochim. Acta* **57,** 2389–2394.

Brown G. E. Jr., Calas G., Waychunas G. A. and Petiau J. (1988) *Rev. Miner.* (*Min. Soc. Am*) **18,** 431–512.

Calas G. and Petiau J. (1983a) *Solid State Comm.* **48,** 625–629.

Calas G. and Petiau J. (1983b) *Bull. Mineral* **106,** 33–55.

Calas G., Bassett W. A., Petiau J., Steinberg M., Tchoubar D. and Zarka A. (1984) *Phys. Chem. Miner.* **11,** 17–36.

Calas G., Brown G. E. Jr., Waychunas G. A. and Petiau J. (1987) *Phys. Chem. Miner.* **15,** 19–29.

Cernik R. J., Murray P. K., Pattison P. and Fitch A. N. (1990) *J. Appl. Crystallogr.* **23,** 292.

Charnock J. M., Garner C. D., Pattrick R. A. D. and Vaughan D. J. (1988) *Phys. Chem. Miner.* **15,** 296–299.

Charnock J. M., Garner C. D., Pattrick R. A. D. and Vaughan D. J. (1989a) *Min. Mag.* **53,** 193–199.

Charnock J. M., Garner C. D., Pattrick R. A. D. and Vaughan D. J. (1989b) *J. Solid State Chem.* **82,** 279–289.

Charnock J. M., Garner C. D., Pattrick R. A. D. and Vaughan D. J. (1990) *Am. Mineral.* **75,** 247–255.

Chen C. T. and Sette F. (1990) *Phys. Scr.* **T31,** 119–126.

Chisholm-Brause C. J., Hayes K. F., Roe A. L., Brown G. E. Jr., Parks G. A. and Leckie J. O. (1990a) *Geochim. Cosmochim. Acta* **54,** 1897–1909.

Chisholm-Brause C. J., O'Day P. A., Brown G. E. Jr. and Parks G. A. (1990b) *Nature* **348,** 528–530.

Cohen A. J. (1985) *Am. Mineral.* **70,** 1180–1185.

Combes J. M., Manceau A., Calas G. and Bottero J. Y. (1989) *Geochim. Cosmochim. Acta* **53,** 583–594.

Combes J. M., Manceau A. and Calas G. (1990) *Geochim. Cosmochim. Acta* **53,** 1083–1091.

Combes J. M., Brown G. E. Jr. and Waychunas G. A. (1991) In *X-ray Absorption Fine Structure, Proc. VIth International XAFS Conference* (Edited by Hasnain S. S.) pp. 312–314. Ellis-Horwood, Chichester.

Cox R. T. (1976) *J. Phys. C,* **9,** 3355–3361.

Cox R. T. (1977) *J. Phys. C,* **10,** 4631–4643.

Cressey G. and Steel A. T. (1988) *Phys. Chem. Minerals* **15,** 304–312.

Cressey G., Henderson C. M. B. and van der Laan G. (1993) *Phys. Chem. Miner.* **20,** 111–119.

Davoli I., Paris E., Stizza S., Benfatto M., Fanfoni M., Gargano A., Bianconi A. and Seifert F. (1992) *Phys. Chem. Miner.* **19,** 171–175.

Dempsey E., Kuhl G. H. and Olsen D. H. (1969) *J. Phys. Chem.* **73,** 387–390.

Dingwell D. B. and Virgo D. (1987) *Geochim. Cosmochim. Acta.* **51,** 195–205.

Dupree R., Kohn S. C., Henderson C. M. B. and Bell A. M. T. (1992) In *Calculation of NMR shielding constants and their use in the determination of the geometric and electronic structures of molecules and solids* (Edited by Tossell J. A.), NATO A.S.I. volume, pp. 421–430.

Farges F. (1991) *Geochim. Cosmochim. Acta* **55,** 3309–3319.

Farges F. and Calas G. (1991) *Am. Mineral.* **76,** 60–73.

Farges F., Ponander C. A. and Brown G. E. Jr (1991a) *Geochim. Cosmochim. Acta* **55,** 1563–1574.

Farges F., Peck J. A. and Brown G. E. Jr. (1991b) In *X-ray Absorption Fine Structure, Proc. VIth International XAFS Conference* (Edited by Hasnain S. S.) pp. 478–480. Ellis-Horwood, Chichester.

Farges F., Sharps J. A. and Brown G. E. Jr. (1993) *Geochim. Cosmochim. Acta* **57,** 1243–1252.

Farges F., Ponader C. W., Calas G. and Brown G. E. Jr. (1992) *Geochim. Cosmochim. Acta* **56,** 4205–4220.

Fei Y. and Mao H. K. (1993) *J. Geophys. Res.* **98,** 11,875–11,884.

Fei Y., Mao H. K., Shu J. and Hu J. (1992a) *Phys. Chem. Miner.* **18,** 416–422.

Fei Y., Mao H. K., Shu J., Parthasarathy G., Bassett W. A. and Ko J. (1992b) *J. Geophys. Res.* **97,** 4489–4495.

Flynn G. J. and Sutton S. R. (1990) *Proc. 20th Lunar Sci. Conf.* 335–342.

Frantz J. D., Mao H. K., Zhang Y.-G., Wu Y., Thompson A. C., Underwood J. H., Giaque R. D., Jones K. W. and Rivers M. L. (1988) *Chem. Geol.* **69,** 235–244.

Fuller C. C., Davis J. A. and Waychunas G. A. (1993) *Geochim. Cosmochim. Acta* **57,** 2271–2282.

Galoisy L. and Calas G. (1991) *Am. Mineral.* **76,** 1777–1780.

Galoisy L. and Calas G. (1992) *Am. Mineral.* **77,** 677–680.

Galoisy L. and Calas G. (1993a) *Geochim. Cosmochim. Acta* **57,** 3613–3626.

Galoisy L. and Calas G. (1993b) *Geochim. Cosmochim. Acta* **57,** 3627–3633.

de Groot F. M. F., Figueiredo M. O., Basto M. J., Abbate M., Petersen H. and Fuggle J. C. (1992) *Phys. Chem. Miner.* **19,** 140–147.

Guttler B., Niemann W. and Redfern S. A. T. (1989) *Min. Mag.* **53,** 591–602.

Hayakawa S., Gohshi Y., Iida A., Aoki S. and Sato K. (1991) *Rev. Sci Instrum.* **62,** 2545–2549.

Hazemann J. L., Manceau A., Sainctavit Ph. and Malgrange C. (1992) *Phys. Chem. Miner.* **19,** 25–38.

Hazen R. M. and Burnham C. W. (1974) *Am. Mineral.* **59,** 1166–1176.

Hazen R. M. and Finger L. W. (1983) *Am. Mineral.* **68,** 595–603.

Helz G. R., Charnock J. M., Vaughan D. J. and Garner C. D. (1993) *Geochim. Cosmochim. Acta* **57,** 15–25.

Henderson C. M. B., Charnock J. M., Helz G. R., Kohn S. C., Pattrick R. A. D. and Vaughan D. J. (1991) In *X-ray Absorption Fine Structure, Proc. VIth International XAFS Conference* (Edited by Hasnain S. S.), pp. 573–578. Ellis-Horwood, Chichester.

Henderson C. M. B., Charnock J. M., Smith J. V. and Greaves G. N. (1993) *Am. Mineral.* **78,** 477–485.

Huggins F. E., Mao H. K. and Virgo D. (1976) *Carnegie Inst. Washington Year b.* **75,** 756–758.

Huggins F. E., Huffman G. P., Mitra S. and Shah N. (1991) In *X-ray Absorption Fine Structure, Proc. VIth International XAFS Conference* (Edited by Hasnain S. S.), pp. 610–612. Ellis-Horwood, Chichester.

Itié J. P. (1992) *High Pressure Res.* **8,** 697–702.

Jackson W. E., Brown G. E. Jr., Waychunas G. A., Mustre de Lyon, J., Conradson S. D. & Combes J. M. (1991) In *X-ray Absorption Fine Structure, Proc. XAFS VI Int. Conf.* (Edited by Hasnain S. S.), pp. 298–301. Ellis-Horwood, Chichester.

Kikegawa T. (1992) *High Pressure Res.* **8,** 631–637.

Kohn S. C., Charnock J. M., Henderson C. M. B. and Greaves G. N. (1990) *Contrib. Mineral. Petrol.* **105,** 359–368.

Kohn S. C., Dupree R., Mortuza M. G. and Henderson C. M. B. (1991) *Phys. Chem. Miner.* **18,** 144–152.

Kopp O. C., Reeves D. K., Rivers M. L. and Smith J. V. (1990) *Chem. Geol.* **81,** 337–347.

Kudoh Y., Prewitt C. T., Finger L. W., Darovskikh A. and Ito E. (1990) *Geophys. Res. Lett.* **17,** 1481–1484.

van der Laan G. and Kirkman I. W. (1992) *J. Phys. Cond. Matter* **4,** 4189–4204.

van der Laan G., Pattrick R. A. D., Henderson C. M. B. and Vaughan D. J. (1992) *J. Phys. Chem. Solids* **53,** 1185–1190.

Loewenstein W. (1954) *Am. Mineral.* **39,** 92–96.

Lu F.-Q., Smith J. V., Sutton S. R., Rivers M. L. and Davis A. M. (1989) *Chem. Geol.* **75,** 123–143.

Manceau A. (1989) *Am. Mineral.* **74,** 1386–1389.

Manceau A. (1990) *Can. Mineral.* **28,** 321–328.

Manceau A. and Combes J. M. (1988) *Phys. Chem. Miner.* **15,** 283–295.

Manceau A., Gorshkov A. I. and Drits V. A. (1992a) *Am. Mineral.* **77,** 1133–1143.

Manceau A., Gorshkov A. I. and Drits V. A. (1992b) *Am. Mineral.* **77,** 1144–1157.

Manceau A., Llorca S. and Calas G. (1987) *Geochim. Cosmochim. Acta* **51,** 105–113.

Manceau A., Bonnin D., Kaiser P. and Takei H. (1988) *Phys. Chem. Miner.* **16,** 180–185.

Manceau A., Bonnin D., Stone W. E. E. and Sanz J. (1990a) *Phys. Chem. Miner.* **17,** 363–370.

Manceau A., Buseck P. R., Miser D., Rask J. and Nahon D. (1990b) *Am. Mineral.* **75,** 490–500.

Mao H. K., Wu Y., Chen L. C. and Shu J. F. (1990) *J. Geophys. Res.* **95,** 21, 737–21, 742.

Mao H. K., Hemley R. J., Fei Y., Shu J. F., Chen L. C., Jephcoat A. P. and Wu Y. (1991) *J. Geophys. Res.* **96,** 8069–8079.

McGetchin T. R. and Besancon J. R. (1973) *Earth Planet. Sci. Lett.* **18,** 408–410.

McKeown D. A. (1989) *Phys. Chem. Miner.* **16,** 678–683.

McKeown D. A. (1991) In *X-ray Absorption Fine Structure, Proc. VIth International XAFS Conference* (Edited by Hasnain S. S.), pp. 346–348. Ellis-Horwood, Chichester.

Mottana A., Paris E., Davoli I. and Anovitz L. M. (1991) *Rend. Lin. Sci. Fis. Nat.* **2,** 379–387.

Nakai I., Akimoto J., Imafuku M., Miyawaki R. and Sugitani Y. (1987) *Phys. Chem. Miner.* **15,** 113–124.

Nelmes R. J. and McMahon M. I. (1994) *J. Synchroton Radiat.* **1,** 69.

Ohkawa M., Yoshiasa Y. and Takeno S. (1992) *Am. Mineral.* **77,** 945–953.

Paris E., Mottana A., Della Ventura G. and Robert J.-L. (1993) *Eur. J. Miner.* **5,** 455–464.

Pattrick R. A. D., van der Laan G., Vaughan D. J. and Henderson C. M. B. (1993) *Phys. Chem. Miner.* **20,** 395–401.

Peacor D. R. (1968) *Z. Kristallogr.* **127,** 213–224.

Pingitore N. E., Lytle F. W., Davies B. M., Eastman M. P., Eller P. G. and Larson E. M. (1992) *Geochim. Cosmochim. Acta* **56,** 1531–1538.

Ponader C. W. and Brown G. E. Jr. (1989a) *Geochim. Cosmochim. Acta* **53,** 2893–2903.

Ponader C. W. and Brown G. E. Jr. (1989b) *Geochim. Cosmochim. Acta* **53,** 2905–2914.

Prewitt C. T., Coppens P., Phillips J. C. and Finger L. W. (1987) *Science* **238,** 312–319.

Putnis A., Salje E., Redfern S. A. T., Fyfe C. A. and Strobl H. (1987) *Phys. Chem. Miner.* **14,** 446–454.

Quartieri S., Antonioli G., Lottici P. P. and Artioli G. (1993) *Min. Mag.* **57,** 249–256.

Rankin A. H. R., Ramsey M. H., Coles B., van Langevelde F. and Thomas C. R. (1992) *Geochim. Cosmochim. Acta* **56,** 67–79.

Redfern S. A. T., Salje E., Marsch W. and Schreyer W. (1989) *Am. Miner.* **74,** 1293–1299.

Redfern S. A. T., Wood B. J. and Henderson C. M. B. (1993) *Geophys. Res. Lett.* **20,** 2099–2102.

Redfern S. A. T., Henderson C. M. B., McGuinn M. D. and Clark S. M. (1993) *Terra Abs.* (Suppl. 1) *Terra Nova* **5,** 364–365.

Rietveld H. M. (1969) *J. Appl. Crystallogr.* **2,** 65–71.

Rivers M. L., Sutton S. R. and Jones K. W. (1991) *Syn. Rad. News* **4,** 23–26.

Ross N. L. and Reeder R. J. (1992) *Am. Mineral.* **77,** 412–421.

Sainctavit Ph., Petiau J., Calas G., Benfatto M. and Natoli C. R. (1987) *J. Phys. C* **9,** 1109–1112.

Sainctavit Ph., Petiau J., Flank A.-M., Ringeisen J. and Lewonczuk S. (1990) *2nd Eur. Conf. Progr. Synchrotron Radiation Res.* **25,** (Edited by Balerna A., Bernieri E. and Mobilio S.), pp. 829–832. SIF, Bologna.

Sainctavit Ph., Calas G., Petiau J., Karnatak R., Esteva J. M. and Brown G. E. Jr. (1986) *J. Phys. C* **8,** 411–414.

Salje E. K. H. (1992) *Phys. Rep.* **215,** 49–99.

Schofield P. F., Henderson C. M. B., Redfern S. A. T. and van der Laan (1993) *Phys. Chem. Miner.* **20,** 375–381.

Seifert F., Paris E., Dingwall D. B., Davoli I. and Mottana A. (1993) *Terra Abs.* (Suppl. 1) *Terra Nova* **5,** 366.

Seward T. M. and Henderson C. M. B. (1992) *29th International Geological Congress*, Kyoto, Japan, Abstract Vol. 3/3.

Seward T. M., Henderson C. M. B., Charnock J. M. and Dobson B. R. (1993) In *Hydrothermal Reactions. Proc 4th International Symposium* (Edited by Cuney M. and Cathelineau M.), pp. 231–233. Institut Lorrain des Geosciences, Nancy, France.

Smith J. V. (1968) *Am. Mineral.*, **53,** 1139–1155.

Stahl K., Kvick A. and Smith J. V. (1988) *J. Solid State Chem.* **73,** 362–380.

Sutton S. R., Jones K. W., Gordon B., Rivers M. L., Bajt S. and Smith J. V. (1993) *Geochim. Cosmochim. Acta* **57,** 461–468.

Torres-Martinez L. M. and West A. R. (1989) *Z. Anorg. Allg. Chem* **573,** 223–230.

Virgo D. and Mysen B. O. (1985) *Phys. Chem. Miner.* **12,** 65–76.

Waldo G. S., Carkson R. M. K., Moldowan J. M., Peters K. E. and Penner-Hahn J. E. (1991) *Geochim. Cosmochim. Acta* **55,** 801–814.

Waychunas G. A. (1987) *Am. Mineral.* **72,** 89–101.

Waychunas G. A. and Brown G. E. Jr. (1990) *Phys. Chem. Miner.* **17,** 420–430.

Waychunas G. A., Apted M. J. and Brown G. E. Jr. (1983) *Phys. Chem. Miner.* **10,** 1–9.

Waychunas G. A., Brown G. E. Jr., Ponader C. W. and Jackson W. E. (1988) *Nature* **332,** 251–253.

Waychunas G. A., Rea B. A., Fuller C. C. and Davis J. A. (1991) In *X-ray Absorption Fine Structure, Proc. VIth International XAFS Conference* (Edited by Hasnain S. S.) pp. 215–217. Ellis-Horwood, Chichester.

Waychunas G. A., Rea B. A., Fuller C. C. and Davis J. A. (1993) *Geochim. Cosmochim. Acta* **57,** 2251–2269.

Weidner D. J., Vaughan M. T., Ko J., Wang Y., Leinenweber K., Liu X., Yeganehhaeri A., Pacalo R. E. and Zhao Y. (1992) *High Pressure Res.* **8,** 617–623.

White R. N., Smith J. V., Spears D. A., Rivers M. L. and Sutton S. R. (1989) *Fuel* **68,** 1480–1486.

Zhang G. and Boduszynski M. M. (1991) In *X-ray Absorption Fine Structure, Proc. VIth International XAFS Conference* (Edited by Hasnain S. S.), pp. 587–589. Ellis-Horwood, Chichester.